



Impact of assimilating thermodynamic and kinematic profiles on a convection initiation forecast

Junkyung Kay^a, Tammy M. Weckwerth^a, David D. Turner^b, Glen Romine^a, Yue Ying^c

^aNSF National Center for Atmospheric Research, Boulder, Colorado

^bNOAA/Global Systems Laboratory, Boulder, Colorado

^cNansen Environmental and Remote Sensing Center, Jahnebakken 3, Bergen, 5007, Norway

Corresponding author: Junkyung Kay, junkyung@ucar.edu

Early Online Release: This preliminary version has been accepted for publication in *Monthly Weather Review*, may be fully cited, and has been assigned DOI 10.1175/MWR-D-24-0233.1. The final typeset copyedited article will replace the EOR at the above DOI when it is published.

© 2025 American Meteorological Society. This is an Author Accepted Manuscript distributed under the terms of the default AMS reuse license. For information regarding reuse and general copyright information, consult the AMS Copyright Policy (www.ametsoc.org/PUBSReuseLicenses).

Abstract

The first field campaign of a network of water vapor lidars, called the MicroPulse Differential absorption lidar (MPD) Network Demonstration Project, combined the observational capabilities of the water vapor MPD, the Atmospheric Emitted Radiance Interferometer (AERI), and the Doppler wind lidar (DWL) at five sites at the Department of Energy (DOE) Atmospheric Radiation Measurement (ARM) Southern Great Plains (SGP) field observatory from 22 April – 19 July 2019. During the field campaign, water vapor profiles from the MPD were collected to complement the ARM/SGP temperature and water vapor profiles from the AERI, wind profiles from the DWL and supplementary radiosondes, along with operational weather radar and surface station data. The impacts of assimilating AERI, MPD, and DWL are evaluated for a mesoscale convection initiation (CI) and precipitation event on 14 June 2019. Short-term forecasts of CI and precipitation are improved by assimilating all MPD and AERI profiling data in comparison to assimilating conventional observations and DWL. While AERI shows marginal impact on the forecasts of CI near the sites, assimilating the MPD water vapor profiles contributes the most to improving forecast skill over almost all forecast times and reflectivity thresholds. The data assimilation (DA) experiments shows the development of moist absolutely unstable layers near the observing sites and MPD DA improved the vertical moisture profile, leading to an improvement of the southern CI forecasts for the MPD DA experiment. Furthermore, MPD DA additionally leads to improved CI forecasts north of the sites due to enhanced thermodynamic instability and modified wind field leading to convergence in the lower atmosphere.

1. Introduction

The atmospheric boundary layer (ABL) impacts society in the form of daily weather occurrence and air pollutant dispersion. Significant efforts have been made to improve the forecasts of the ABL, including generation of accurate initial conditions (Zhang et al. 2006; Snook et al. 2011; Romine et al. 2013; Stensrud et al. 2013; Johnson et al. 2015; Wheatley et al. 2015; Jones et al. 2016), better formulations to represent surface and turbulent processes (Sandu et al. 2013), and more accurate simulations of mesoscale and large-scale dynamics (Chan et al. 2023). To achieve these improvements, the necessity of high spatiotemporal resolution observations within and above the ABL has increased to measure the structure and evolution of the ABL and to analyze initial conditions for predictions (Coniglio et al. 2013; Romine et al. 2013; Sobash and Stensrud 2015). Turner et al. (2019) and Wulfmeyer et al. (2015) suggested that dynamic and thermodynamic profiles at 15 minute or better frequency and data vertical grid spacings of 100 m or less are needed to resolve the atmospheric state of the ABL for accurate analyses for improved forecasting skill.

Sufficient water vapor in the low troposphere is one key ingredient for thunderstorm initiation (Johns and Doswell 1992; Holley et al. 2014). The positive horizontal advection of higher water vapor into the ABL can enhance atmospheric instability, affecting prediction of the likelihood of severe weather occurrences (Crook 1996; Ducrocq et al. 2002; Richard et al. 2007; Keil et al. 2008; Dierer et al. 2009; Wulfmeyer et al. 2011). The water vapor often varies substantially on horizontal scales as small as 1-2 km, which is partly attributed to the structure and evolution of the ABL (Weckwerth et al. 1996), and the ABL circulations associated with these moisture variations may lead to convection initiation (CI) (Weckwerth 2000). The temporal variability of water vapor has a timescale of minutes to hours in the ABL and in the free troposphere located above the ABL, respectively (Vogelmann et al. 2015). The current nationwide observational network for water vapor profiles consists of radiosonde and aircraft observations, whose horizontal spacings are too sparse to resolve the rapid spatiotemporal changes of water vapor. Due to their global coverage over the land and high-resolution in the vertical direction, radiosondes have been assimilated operationally and show significant positive impacts on global and regional weather forecasting (Ingleby et al. 2016; Sato et al. 2017). However, the low temporal resolution of operational radiosonde networks, typically having twice daily soundings,

coupled with their coarse ~300 km spacing, limits their ability to represent the rapid evolution of ABL structure and CI processes. Aircraft observations show the most substantial impact of all operational observations on 6-hour forecasts in the troposphere using the hourly updated Rapid Refresh (RAP) numerical weather prediction (NWP) data assimilation (DA) system (James and Benjamin 2017). Aircraft only provide ABL observations during their takeoffs and landings near airports, so the lack of spatial and temporal coverage of the aircraft observations prevent them from providing continuous observations in the ABL throughout the entire diurnal cycle. Furthermore, most aircraft only provide temperature and wind data; only a small fraction (order 10%) provide water vapor observations (Petersen 2016; Petersen et al 2016).

To partially fill the spatiotemporal gaps of water vapor observations in ABL, the National Science Foundation National Center for Atmospheric Research (NSF NCAR) and Montana State University (MSU) jointly developed a water vapor profiling instrument called MicroPulse Differential absorption lidar (MPD). MPD is a compact, active water vapor lidar that utilizes a commercially-available micropulse laser. The MPD has advanced features using a low-cost and eye-safe laser and has unattended operation capability with uniform high resolution in the low troposphere (Spuler et al. 2015; Stillwell et al. 2020; Spuler et al. 2021). The MPDs used in this study were able to observe water vapor profiles above 700 m AGL, but recent MPD improvements have lowered the minimum altitude to 200-300 m. Previous studies showed the consistent quality of MPD profiles compared with those from radiosondes and showed improved representation of elevated moist layers compared to Atmospheric Emitted Radiance Interferometer (AERI) and microwave radiometer profiles (Weckwerth et al. 2016). Assimilating synthetic MPD water vapor profiles that were collocated with the operational radiosonde sites had substantial positive impact on the prediction of a nocturnal CI event in an Observing System Simulation Experiment (OSSE) framework (Kay et al. 2022). Using the OSSE, Kay et al. (2022) also demonstrated the potential configuration of a nationwide MPD network showing better quantitative precipitation forecasting (QPF) skill (Roberts and Lean 2008) than the radiosonde network alone over the U.S.

The MPD Network Demonstration project collected data within the DOE/ARM/SGP array (Sisterson et al. 2016) from five sets of MPD, AERI, and Doppler wind lidar (DWL) (Fig. 1) from 22 April 2019 to 19 July 2019. Although an OSSE is an effective method to estimate the potential

benefits of newly developed instruments, the MPD effect in OSSEs could be exaggerated compared to the actual MPD observation impact because of potential underestimation of model errors and overestimation of observation errors in OSSEs (Privé and Errico 2013; Kay et al. 2022). Therefore, following Kay et al. (2022), the actual impact of MPD water vapor profiles on a CI and evolution forecast is investigated in this study.

The main goal of this study is to demonstrate the impact of assimilating actual MPD water vapor, AERI temperature and water vapor, and DWL wind profiles collected during the MPD network demonstration project. We chose a nocturnal CI and early evolution event that fortuitously occurred near the observing sites to assess the observation impact of assimilating collocated ABL temperature, water vapor, and wind profiles on QPF skill. Because these assimilated profiles are located 50-60 km apart, this study mainly focuses on the effects of MPDs, AERIs and DWLs on local thermodynamic and kinematic variability and consequently on precipitation forecasting in a limited region. The prediction of thunderstorm initiation and evolution can be improved by better analyses of the near-storm environment (e.g., Hu et al. 2023). For example, necessary conditions for thunderstorm development include both dynamic and thermodynamic components associated with moisture, conditional instability, lifting and vertical wind shear (e.g., Thompson et al. 2003; Craven and Brooks 2004; Schneider and Dean 2008). Previous studies have demonstrated the benefits of assimilating both wind profiles from DWL and thermodynamic profiles from AERI to improve forecasts of the initiation and evolution of thunderstorms (Coniglio et al. 2019; Hu et al. 2019; Degelia et al. 2019; Degelia et al. 2020; Chipilski et al. 2020, 2022). Hu et al. (2019) demonstrated that assimilation of DWL and AERI improves short-term probabilistic forecasts of a tornadic supercell event by increasing low-level convergence and the moisture in the lower atmosphere. Following results from previous studies, we evaluate the combined effect of MPD water vapor profiles and the DWL and AERI profiles on a CI and early evolution event.

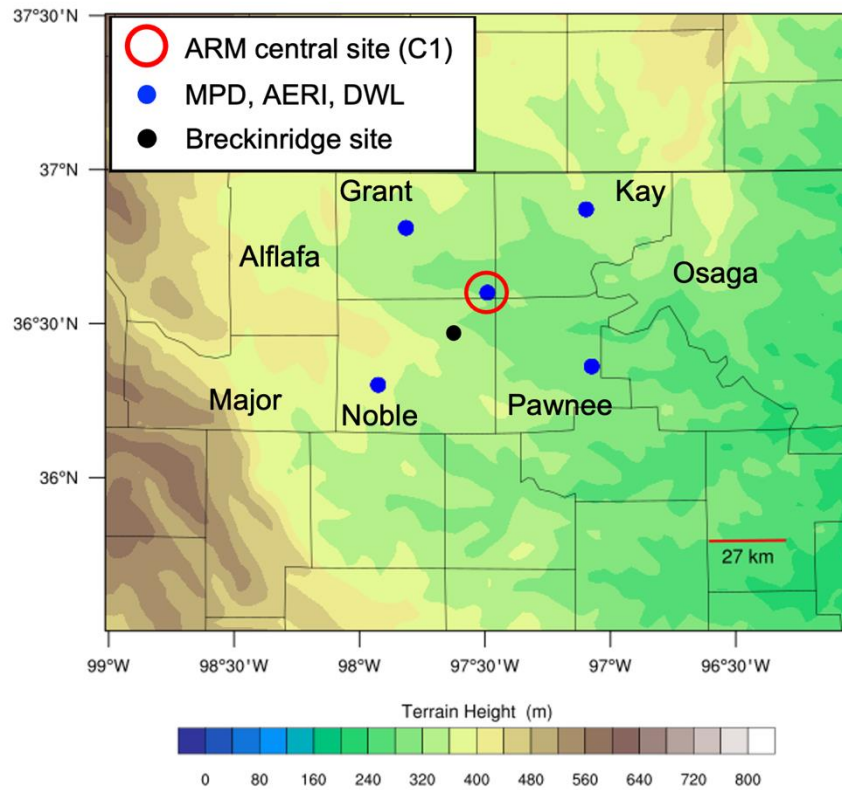


Figure 1. Map of deployment sites at ARM/SGP and Breckinridge, Oklahoma mesonet site in northern Oklahoma during the MPD network demonstration project. ARM radiosondes were launched every 3 hours from C1 during this event. The names of the counties around the observation points were also shown.

This paper is organized as follows. Section 2 describes the convective event in detail. Section 3 introduces observations used in the MPD demonstration project, which include MPD, AERI, and DWL, and describes their observation errors used for the DA experiments. Section 4 explains the model and DA system and the experimental design. Section 5 shows the results of assimilating the thermodynamic profiles from MPD and AERI and wind profiles from DWL. Section 6 contains a summary and discussion.

2. Case description

Figure 2 shows the radar reflectivity evolution of the convection event. At 0300 UTC 14 June 2019, a squall line was observed across western Nebraska extending into northeastern Colorado, and mesoscale convective systems (MCSs) were found near the panhandles of Oklahoma and

Texas (Fig. 2a). These convective systems moved southeastward and new convective cells were initiated in north-central Oklahoma and south-central Kansas ahead of the pre-existing convection at 0515 UTC 14 June 2019 (Fig. 2b). Convective cells continued to initiate and they organized into two parallel bands while moving southeastward (Figs. 2c, d). The newly developed convective systems merged with the pre-existing convection that extended through central Kansas (Fig. 2e). After 0800 UTC, the merged system formed a squall line extending from southern Nebraska through Kansas and central Oklahoma (Fig. 2f).

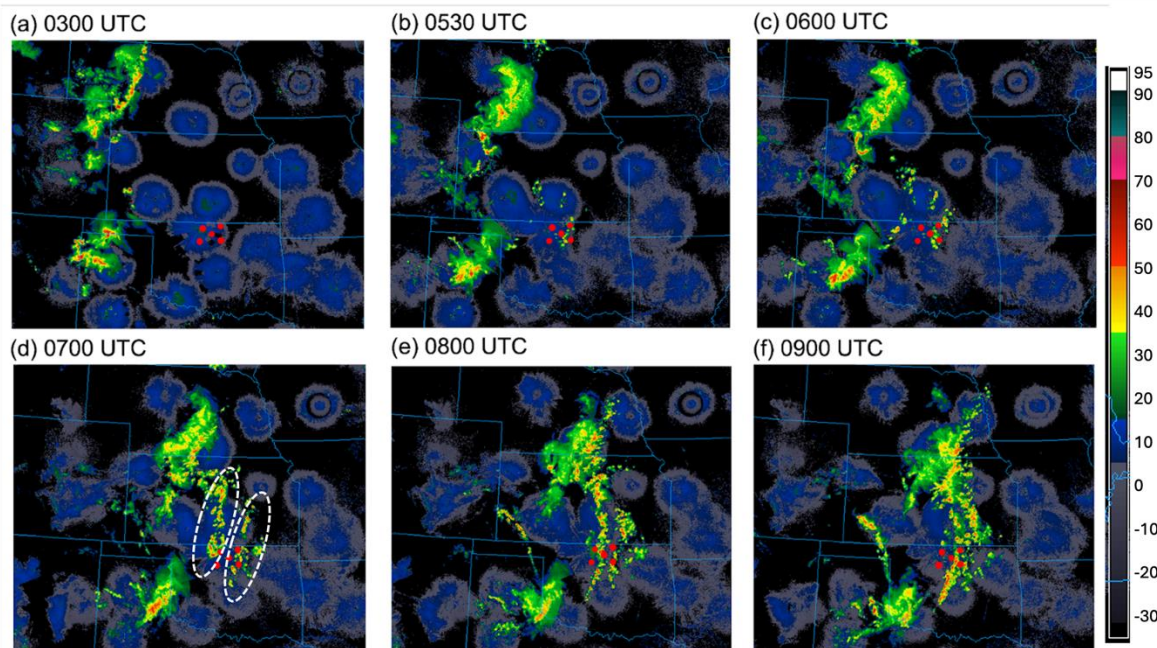
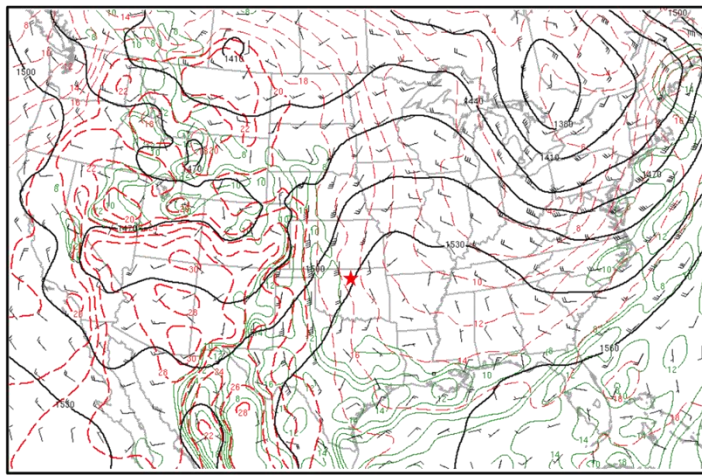


Figure 2. (a) Composite reflectivity (dBZ; color fill) at (a) 0300 UTC, (b) 0530 UTC, (c) 0600 UTC, (d) 0700 UTC, (e) 0800 UTC, and (f) 0900 UTC 14 June 2019. The red dots indicate the location of the profilers at the ARM/SGP sites. The white dashed ellipses in Figure 2d refer to the two parallel bands mentioned in the text. The radar reflectivity observations are provided from the NSF NCAR/MMM image archive (<https://www2.mmm.ucar.edu/imagearchive>).

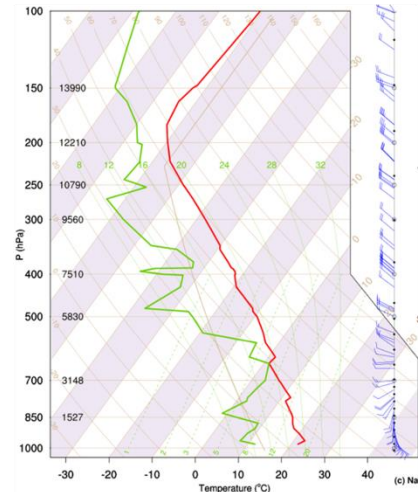
The National Oceanic and Atmospheric Administration (NOAA) National Center for Environmental Prediction (NCEP) Storm Prediction Center (SPC) analysis at 0300 UTC 14 June 2019 at 850 hPa and 700 hPa show that water vapor was likely transported eastward to western Oklahoma and western Kansas (Fig. 3a, e) above 700 hPa. There was also a prominent thermal gradient in western Kansas, Oklahoma, and Texas associated with a broad low-pressure region over the western U.S. (Fig. 3a). The 500 hPa analysis shows that a weak ridge over the Rockies

and a trough over the eastern U.S. developed with a northwesterly wind over Oklahoma and Kansas at 0300 UTC 14 June 2019 (not shown). At 0600 UTC after the new convection initiated near the OK/KS border, the 500 hPa upper-level (not shown) and 850 hPa low-level analyses have features similar to those at 0300 UTC (Fig. 3c). There was minimal change in water vapor at the ARM/SGP site around 850 hPa from 0300 UTC to 0600 UTC (Figs. 3a and c). The horizontal gradient of water vapor, oriented perpendicular to the wind vectors, suggests that water vapor gradually spread eastward from western Oklahoma and Kansas into the ARM/SGP site rather than being directly transported into the ARM/SGP sites by the LLJ (Fig. 3c). The soundings at the Central Facility (C1 site) near Lamont, Oklahoma show a substantial increase in the low-to-mid level relative humidity (RH) between 750 hPa to 450 hPa from 0300 UTC to 0600 UTC (compare Figs. 3b and d), likely due to ascent associated with the 700 hPa warm advection (Fig. 3e). Figure 4 shows the time series of surface observations provided by the Oklahoma mesonet at Breckinridge, which is the station closest to the observing sites of the field campaign. The surface conditions are characterized by a weak southeasterly wind of about 6 m s^{-1} and only small RH and pressure changes during 0300-0500 UTC when the data assimilation was performed. Neither the surface station data nor the low-level NEXRAD radar data (not shown) from Wichita (KICT) and Vance Air Force Base (KVNX) showed an obvious low-level boundary prior to the CI.

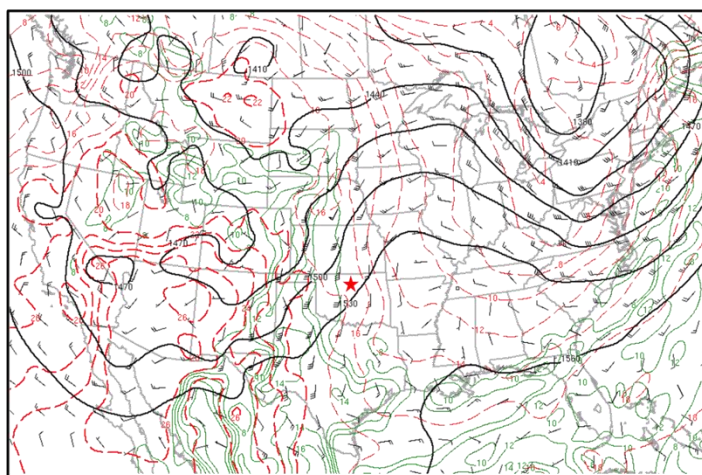
(a) 850 hPa analysis (0300 UTC)



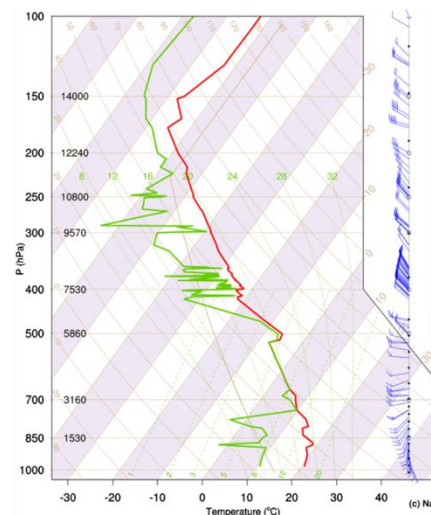
(b) Sounding (0300 UTC)



(c) 850 hPa analysis (0600 UTC)



(d) Sounding (0600 UTC)



(e) 700 hPa analysis (0500 UTC)

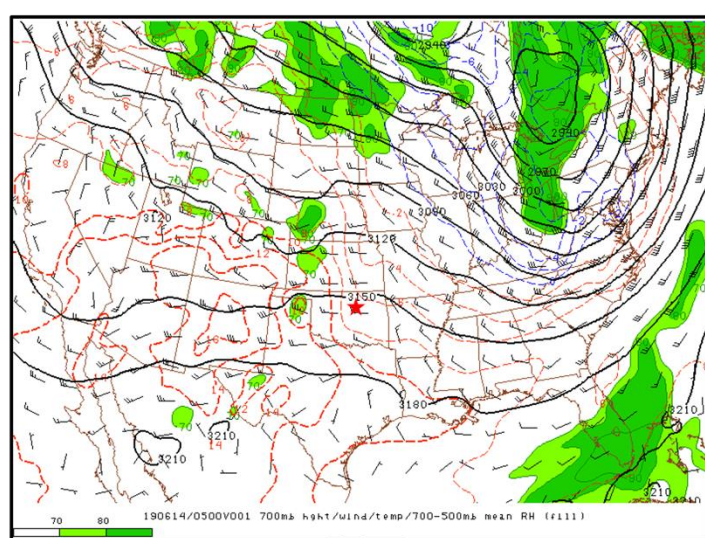


Figure 3. (a) 850 hPa geopotential height (m; black contours), temperature ($^{\circ}$ C; red contours), dew point temperature ($^{\circ}$ C; green contours), wind (knots; barbs) valid at 0300 UTC 14 June and (b) sounding observation from Lamont, OK at 0300 UTC 14 June 2019. (c) and (d) are the same as (a) and (b) but for 0600 UTC 14 June 2019. (e) is the same as (a) but for 0500 UTC 14 June 2019 at 700 hPa. Red stars in (a), (c) and (e) indicate the location of the Lamont, OK C1 sounding observations in (b) and (d).

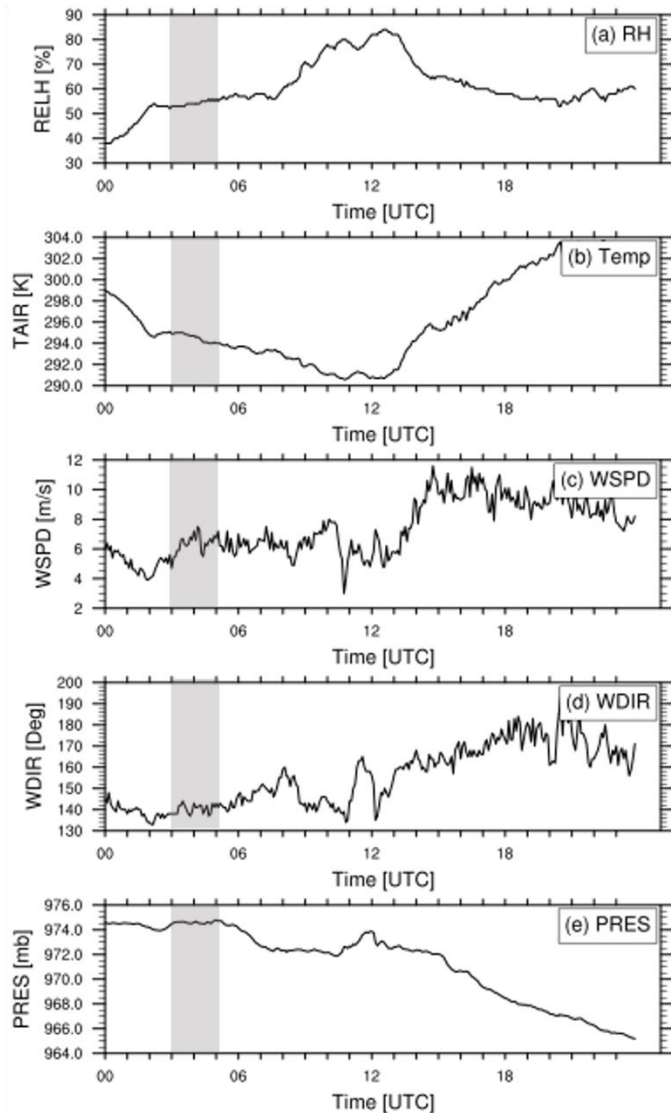


Figure 4. Time series of (a) 2-m relative humidity (%), (b) 2-m temperature (K), (c) 10-m wind speed ($m s^{-1}$), (d) wind direction ($^{\circ}$) and (e) surface pressure (hPa) from Oklahoma mesonet at Breckinridge. The mesonet station observations are provided from (<https://www.mesonet.org/>). The gray shading indicates the DA period from 0300 UTC to 0500 UTC 14 June 2019.

3. MPD network demonstration project observations

a. Observations

The MPD, AERI, and DWL observations on 14 June used in this study were collected from the MPD network demonstration project (UCAR/NCAR-Earth Observing Laboratory 2019; ARM user facility 2016; ARM user facility 2010). MPD is a micropulse, diode-laser-based, differential absorption lidar for water vapor profiling in the lower troposphere. The design at its early development stage is described in Spuler et al. (2015), and the validation results of the MPD with other water vapor profiling measurements are discussed in Weckwerth et al. (2016). The typical range of the observed water vapor profiles from the MPDs in this campaign was from 700 m to 5 km AGL in clear sky conditions (Table 1). The MPD in this study could not accurately measure water vapor profiles below 700 m due to contamination from the outgoing pulse. Because the signal of MPD cannot penetrate optically thick clouds, the vertical range of the MPD is reduced during cloudy conditions (Spuler et al. 2015; Spuler et al. 2021). The MPD produces profiles with 150-m vertical spacing every 5 minutes.

The AERI is a passive hyperspectral infrared radiometer that measures downwelling infrared radiance from the atmosphere (Knuteson et al. 2004). The vertical profiles of temperature and water vapor are retrieved by the TROPoE (formerly AERIoe) retrieval algorithm (Turner and Löhnert 2014; Turner and Blumberg 2019). The vertical range of reliable data in AERI profiles is from 10 m to 2 km AGL in clear air conditions; above 2 km the retrieved profiles are less reliable. The temporal frequency of AERI is 1 minute, and the vertical spacing of the raw data decreases rapidly with height, having 10 m and 200 m resolutions near the surface and 2 km AGL, respectively (Weckwerth et al. 2016).

The DWL measures the horizontal wind profiles in the lower troposphere using the optical Doppler effect (Pearson et al. 2009; Hanesiak and Turner 2016) based on the velocity-azimuth-display (VAD) algorithm (Browning and Wexler 1968). DWL operates in the near infrared (1.5 μm) and ranges from 90 m to 3 km in height with 30 m vertical spacing every 15 minutes. The vertical range of DWL is affected by aerosol backscatter, humidity, precipitation and atmospheric refractive turbulence (Aitken et al. 2012). The detailed description of instruments during the campaign is summarized in Table 1.

Table 1. Instruments used in this study.

Instrument	Measured variables	Vertical range	Resolution	Instrument accuracy
MPD	Absolute humidity (g m^{-3})	700 m – 5 km*	150 m /5 min	1 g m^{-3}
AERI	Water vapor mixing ratio (g kg^{-1}), Temperature (K)	10 m – 2 km*	10 m – 2 km/ 1 min	0.8 g kg^{-1} , 1°C
DWL	Horizontal and vertical wind profiles (m s^{-1})	90 m – 3 km*	30 m/15 min	1 m s^{-1}

*These remote sensing systems can only profile up to the base of clouds as most clouds are opaque to the lidar and AERI, limiting the range to that stated or cloud base height, whichever is lower.

Figure 5 shows the time series of the stage4 1-hr accumulated precipitation (Lin and Michell 2005) and the vertical profiles from the MPD, AERI, and DWL at the C1 site (Fig. 1). The precipitation that began after 0530 UTC 14 July 2019 affected the effective vertical range of the instruments for this event. For example, MPD cannot retrieve the backscattered signal above 2.2 km AGL when there was a cloud passage from 0300 UTC to 0800 UTC 14 June. The base of the MPD profile used for this study is 700 m AGL, which was determined due to contamination of water vapor estimates near the surface that result primarily from the remnant effect of the outgoing pulse from MPD. This limit pertains to this dataset, and recent improvements to the MPD have lowered the minimum altitude for reliable data to 200-300 m (Stillwell et al. 2020). In contrast, AERI can measure mixing ratio profiles from near surface to below 1 km AGL during the same period (Fig. 5c). The limited range of AERI compared to MPD is due to different types of remote sensing (passive vs. active) and severe contamination of infrared radiance of AERI in moist convective regions where clouds dominate radiation fluxes. The higher vertical range of MPD leads to better representation of elevated moisture layers that were evident at 2.8 km at 00 UTC and at 1.2 km after 03 UTC 14 June (Fig. 5b), whereas the AERI was unable to represent these layers due to its coarser vertical resolution at those heights. The horizontal wind from DWL was available up to 1.3 km AGL. Table 2 shows the correlation coefficients of wind and thermodynamic variables between each profiler and the radiosonde located at the C1 site at 0300

UTC and 0600 UTC on 14 June 2019, and shows the reliability of all profilers based on the comparisons to the radiosonde during the pre-convective and early convection time period.

Table 2. Correlation coefficient between profiles and radiosonde at C1 site at 0300 UTC and 0600 UTC 14 June 2019.

	DWL U-wind	DWL V-wind	AERI water vapor	AERI temperature	MPD water vapor
Correlation coefficient	0.92	0.89	0.78	0.89	0.81

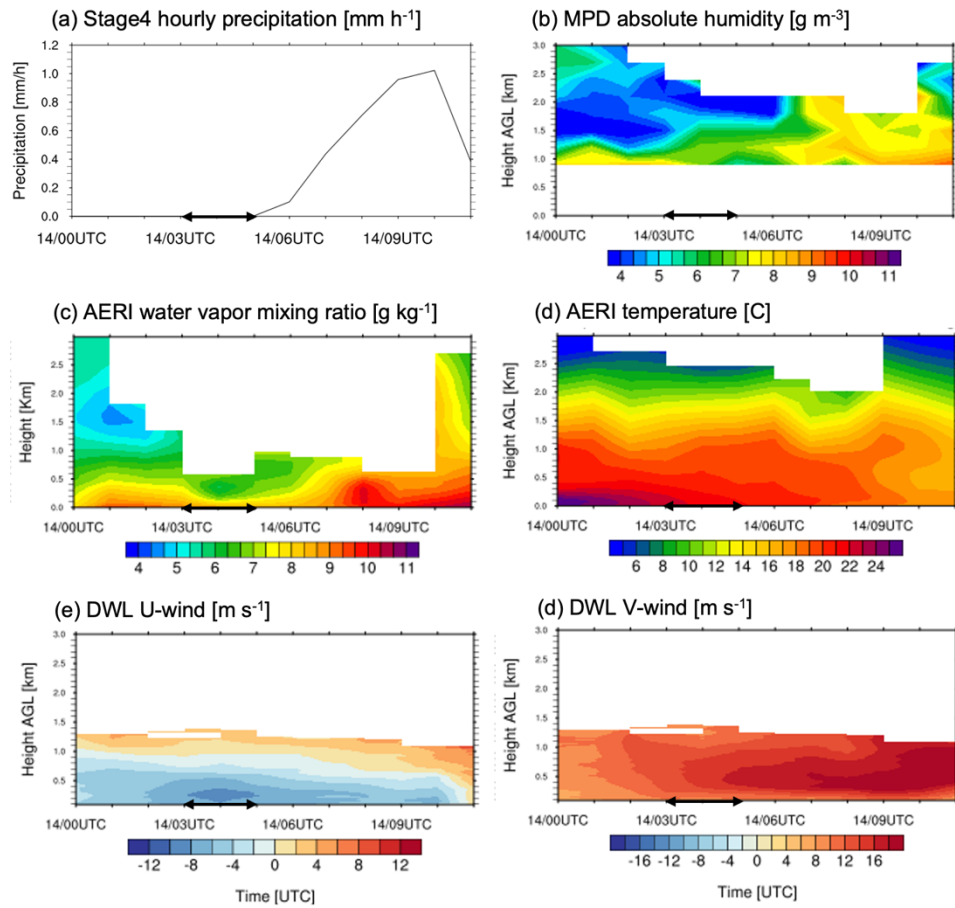


Figure 5. Time series of (a) stage4 hourly precipitation (mm h^{-1}), (b) absolute humidity from MPD (g m^{-3}), (c) water vapor mixing ratio from AERI (g kg^{-1}), (d) temperature from AERI ($^{\circ}\text{C}$), (e) zonal wind component from DWL (m s^{-1}) and (f) meridional wind component from DWL (m s^{-1}) at the C1 site from 0000 UTC to 1200 UTC 14 June 2019. The white regions represent missing data. The black arrow indicates the DA period from 0300 UTC to 0500 UTC 14 June 2019.

In this study, we assimilated conventional observations including radiosonde, aircraft observations, and surface station data (Fig. 6) in addition to the profiling data from the MPD demonstration project (Fig. 5) into the Weather Research and Forecasting (WRF-ARW) model (model details are described in section 4a). The conventional observations are provided by the NCEP operational Global Data Assimilation System (GDAS). We used the standard Gridpoint Statistical Interpolation (GSI) system observation errors for assimilating conventional observations (Shao et al. 2016; Hu et al. 2018).

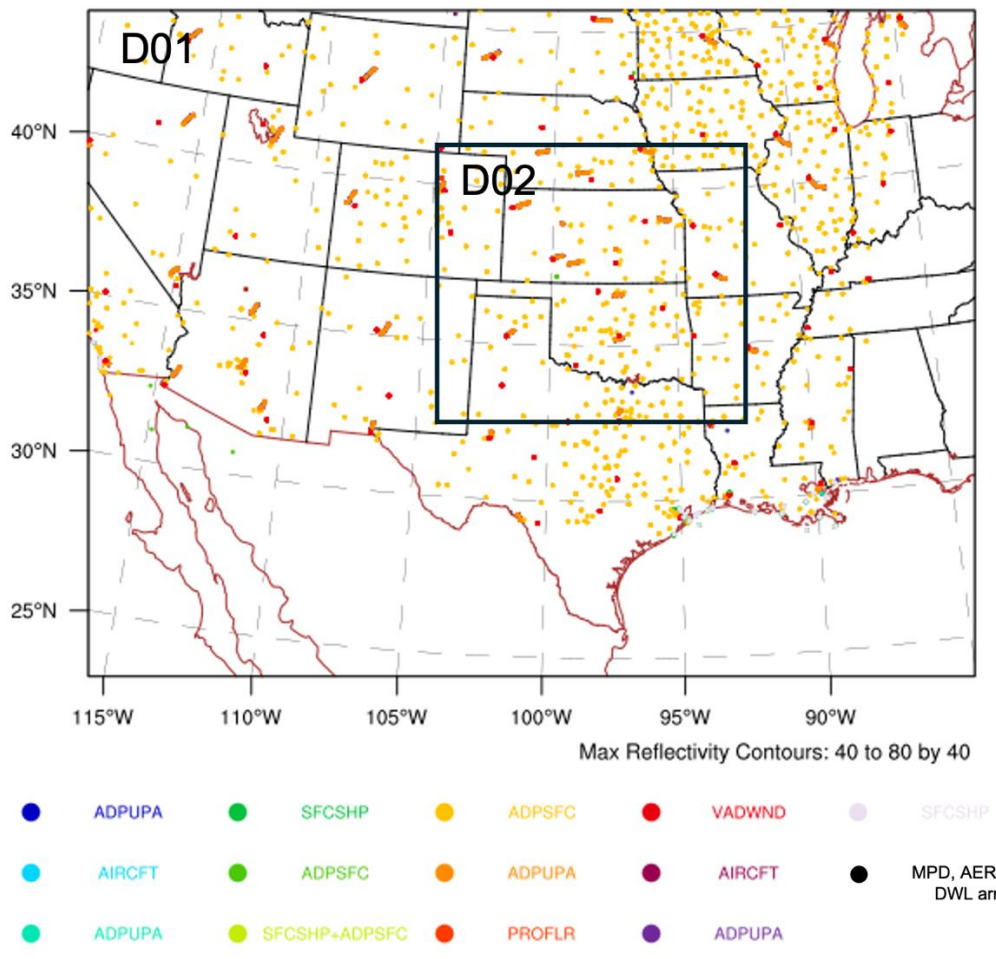


Figure 6. Horizontal distribution of observations assimilated in this study and model domain (D01 and D02). Black dots represent the locations of the five MPD, AERI and DWL profilers. ADPUA represents upper air sonde report, AIRCFT represents aircraft flight level report, SATWND represents satellite-derived winds report, VADWND represents NEXRAD wind report, ADPSFC represents surface land report, SFCSHP represents surface marine report, and PROFLR represents wind profiler report.

b. Treatment of observation error

Observation error is one critical factor in determining the weights of observations and model background in DA. To produce accurate analyses and forecasts, the observation error should represent the uncertainties associated with instrumental accuracy and discrepancies between model resolutions and observation coverages in space and time. The former is called instrument error and the latter is called representativeness error (Geer and Bauer 2011; Janjić et al. 2017). In this study, we used the observation errors from Degelia et al. (2019) that estimated the AERI and DWL observation errors using the dataset collected from the Plains Elevated Convection at Night (PECAN) experiment (Geerts et al. 2017). Kay et al. (2022) estimated the vertical profile of MPD observation error following the general approach of Degelia et al. (2019) that was used for the AERI and DWL. Degelia et al. (2019) quantified the observation errors by combining the instrument error and inflated residual error profiles of rawinsondes. More detailed descriptions regarding AERI and DWL observation errors can be found in Degelia et al. (2019). Figure 7 shows the observation errors for MPD, AERI, and DWL used in the current study. The MPD observation error increases with height above 1.2 km AGL due to relatively strong backscatter gradient, weak signal-to-noise ratio and the effect of clouds that reduce the MPD observation confidence in high altitude (Kay et al. 2022). Because this is the first study to assimilate real profiles from MPD and evaluate its impact on precipitation forecasting skill, we use those observation errors as first guesses, and more accurate observation errors for MPD, AERI, and DWL will be quantified using more sophisticated approaches such as the residual-based method (Hollingsworth & Lönnberg, 1986; Desroziers, 2005) in the future.

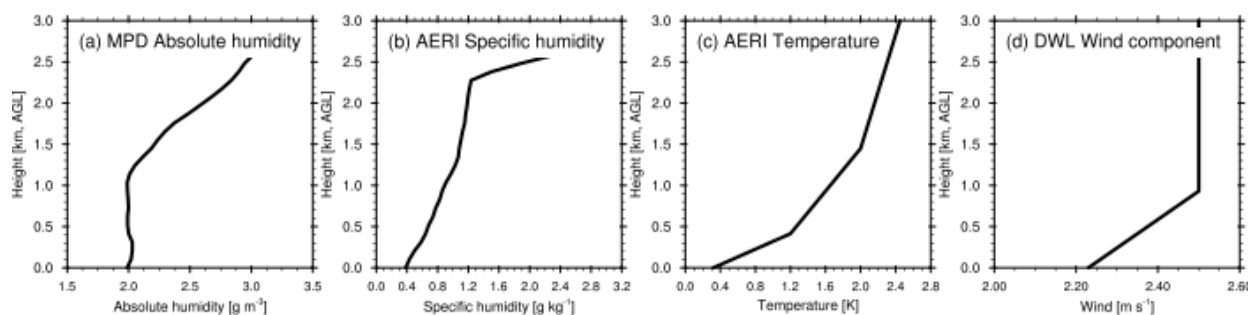


Figure 7. Observation error profiles for (a) MPD absolute humidity (g m^{-3}), (b) AERI specific humidity (g kg^{-1}), (c) AERI temperature ($^{\circ}\text{C}$), and (d) DWL wind component (m s^{-1}).

4. Methods

a. Model and data assimilation system

For this case study, we perform numerical simulations using the convection-permitting Advanced Research version of WRF-ARW model version 4.1.2 (Skamarock et al. 2008; Powers et al. 2017). Two nested domains were configured using 15 km (D01) and 3 km (D02) horizontal grid spacings, and both domains have 71 vertical levels reaching the model top of 50 hPa (Fig. 6). The physical parameterization schemes used in this study are summarized in Table 3. It is noted that simulations on D02 allow the model to begin resolving convection so the cumulus parameterization is not utilized in D02.

Table 3. Configuration of model physical parameterizations used in this study.

Microphysical parameterization	Thompson microphysics (Thompson et al. 2008)
Cumulus parameterization	Kain-Fritsch (Kain and Fritsch 1990, 1993; Kain 2004; Only for outer domain D01)
PBL parameterization	Mellor–Yamada–Janjic (MYJ) (Janjić 2002)
Land Surface Model parameterization	Noah land surface model (Chen and Dudhia 2001)
Longwave radiation parameterization	Rapid Radiative Transfer Model for Global Climate Models (RRTMG; Mlawer et al. 1997; Iacono et al. 2008)
Shortwave radiation parameterization	RRTMG

To demonstrate observation impact from the ABL profilers, we conduct DA experiments using the Ensemble Adjustment Kalman Filter (EAKF) system within the Data Assimilation Research Testbed (DART; Anderson et al. 2009). Many previous studies demonstrated the capabilities of the DART system for convective-scale DA (e.g., Kerr et al. 2017; Schwartz et al. 2015, 2019; Kay et al. 2022). To alleviate sampling error issues caused by the limited ensemble sizes, the DART utilizes inflation factors and covariance localization techniques. For covariance localization, the spurious correlation estimated by the analysis ensemble is tapered by using the Gaspari and Cohn (1999) function. The horizontal localization radius is 300 km and the vertical localization radius is 2 km for both D01 and D02. These radii are chosen based on the previous

studies assimilating similar conventional and research-grade observations (e.g., Degelia et al. 2019; Coniglio et al. 2019; Kay et al. 2022). To avoid catastrophic filter divergence in the ensemble-based DA system, spatially varying inflation factors are applied to the DART ensembles. In this study, the reduced posterior ensembles were relaxed to 85% of the prior ensemble by the inflation factors (Whitaker and Hamill 2012; Kay et al. 2022).

For the initial conditions (ICs) and lateral boundary conditions (LBCs) at the beginning of DA cycles, we generate a 50-member ensemble for the outer domain D01 by adding random perturbations to the NCEP Final (FNL) analysis valid at 1800 UTC 12 June 2019. The random perturbations are drawn from the climatological forecast error covariance of the WRF three Dimensional Variational (3DVAR) DA system (Barker et al. 2004; Torn et al. 2006; Wang et al. 2008). We downscale these 15-km outer domain conditions to provide the ICs and LBCs for the 3-km inner domain members valid at 1800 UTC 12 June 2019. These ensemble members were then integrated for 6 hours spin-up for both D01 and D02 to form the background ensemble for cycling DA experiments.

b. Experimental design

Figure 8 shows the timeline for the DA experiments in this study. All conventional observations were assimilated from 0000 UTC 13 June to 0300 UTC 14 June 2019 with 3-hourly intervals on both D01 and D02 simultaneously. The detailed procedure to generate the background ensemble at the beginning of DA cycles valid at 0000 UTC 13 June 2019 was presented in section 4a. The conventional observations within the 1-hour window straddling each analysis time were assimilated assuming they were valid at that central time, and the resulting analysis ensemble was integrated for 3 hours to provide the background ensemble for the subsequent 3-hourly DA cycle. We conducted a sensitivity test of assimilating the conventional observations collected within a 1.5-hour window straddling each analysis time from 0000 UTC 13 June to 0300 UTC 14 June 2019 with 3-hourly intervals. The results showed that the analysis and forecast, after assimilating MPD water vapor profiles using the background ensemble from the 3-hourly DA cycle, produced overestimated convection that extended further southward compared to forecasts using the background ensemble with a 1-hour window (not shown). This comparison suggests that an excessively long assimilation window for conventional observations can lead to suboptimal

background ensembles for assimilating MPD profiling data. The degradation is primarily due to the inclusion of conventional observations, particularly surface station data, that are less relevant to the analysis time.

We assimilated the profiling observations and conventional observations from 0300 UTC 14 June 2019 to 0500 UTC 14 June 2019 with 15-minute intervals on both D01 and D02. For optimal assimilation of AERI profiles, we used AERI data below the cloud base height and thinned the AERI profile corresponding to the cumulative degrees of freedom following Turner and Blumberg (2019). To reduce correlated observation errors, we averaged the profiling observations over a 10-hPa depth, following Degelia et al (2019). This method is only used for the section of the profile where the raw observation spacing is smaller than 10-hPa. Temporal averaging is not applied. Profiling observations and conventional observations within the 7.5-minute window straddling the analysis time were assimilated for the 15-minute DA cycles (Table 4). The CNTL experiment assimilates DWL wind profiles and conventional observations including radiosonde, aircraft observations and surface station data. Three additional DA experiments were conducted to evaluate the impact of assimilating thermodynamic profiling observations (i.e., AERI and MPD) in addition to the conventional observations and DWL. We have also conducted sensitivity tests of the DA frequency for profiling observations varying the DA cycling interval from 5 minutes to 60 minutes from 0300 UTC 14 June to 0500 UTC 14 June 2019. We chose to use 15-minute DA intervals because they showed the most reliable results in terms of the reflectivity forecasts (not shown). This might be due to the overestimated CI and its evolution by frequent update of analysis and resultant model imbalance, consistent with results of Ying and Wang (2023).

Thorough sensitivity tests of assimilating conventional observations and DWL wind profiles showed negligible impacts of DWL on analyses and forecasting skills compared to assimilating only conventional observations. This is because the background wind field was so accurate that the correction of the background wind field by assimilating DWL wind profiles was marginal in this case. The magnitude of the wind analysis increment is less than 0.5 m s^{-1} at 0.8 km AGL (Figs. 9a and 9b), which is two orders of magnitude smaller than the prevailing wind of approximately 17 m s^{-1} (Fig. 9d). The difference between DWL profiles and background wind

profiles is substantially smaller than the DWL observation error (Fig. 7d), resulting in the small increments on wind analyses. Therefore, DA experiments assimilating only conventional observations and both conventional observations and the DWL (CNTL) result in similar analyses and forecasts. Due to the insignificant observation effect of DWL wind profiles on analyses and forecasts, we will focus on the effect of assimilation of thermodynamic profiles from MPD and AERI by comparing CNTL_AERI and CNTL_MPQ experiments with CNTL experiments. Finally, the combined effects of assimilating AERI and MPD thermodynamic profiles with DWL wind profiles will be assessed in the ALL experiment. It is noted that the result of assimilating only conventional observations is not discussed further.

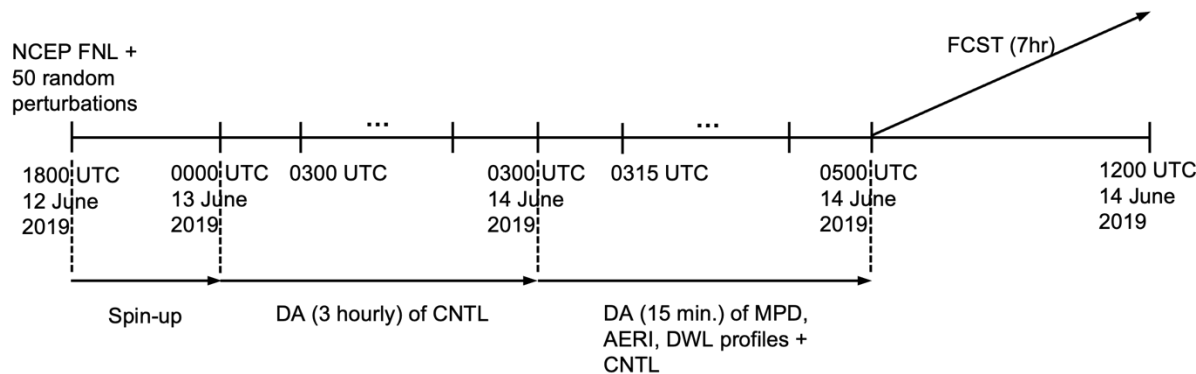


Figure 8. Illustration of the DA timeline.

Table 4. Experimental configuration for data assimilation. Conventional observations include radiosondes, aircraft observations, and surface station data. DWL measures horizontal wind profiles [m s^{-1}], AERI measures temperature [$^{\circ}\text{C}$] and water vapor mixing ratio [g kg^{-1}] profiles, and MPD provides absolute humidity [g m^{-3}] profiles.

Experiment	Observations
CNTL	Conventional observations + DWL wind profiles
CNTL_AERI	Conventional observations + DWL wind profiles + AERI T and Q profiles
CNTL_MPQ	Conventional observations + DWL wind profiles + MPD Q profiles
ALL	Conventional observations + DWL wind profiles + AERI T and Q profiles + MPD Q profiles

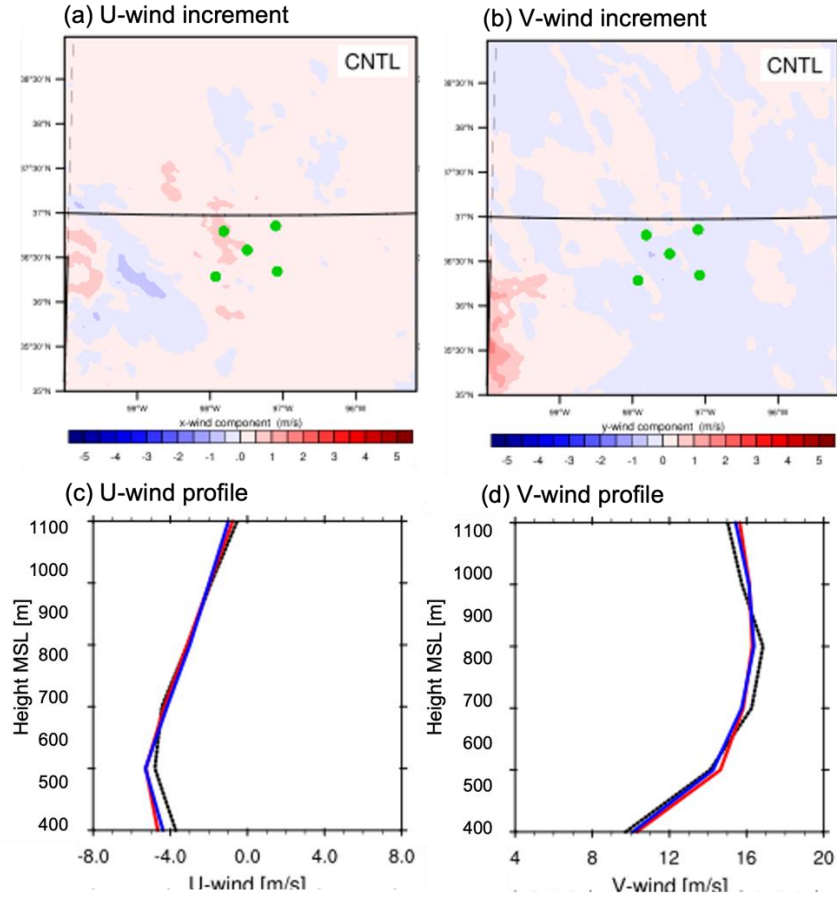


Figure 9. Analysis increment of CNTL experiment for (a) zonal wind and (b) meridional wind at 0.8 km AGL valid at 0500 UTC 14 June 2019. Vertical profiles of ensemble mean analysis (blue), ensemble mean background (red) and DWL wind profiles (black) for (c) zonal wind and (d) meridional wind components valid at 0500 UTC 14 June 2019. The green dots in (a) and (b) indicate the location of the profilers.

5. Results

a. Overview of the analysis and forecasts

In this section, we will demonstrate the overall impact of assimilating lower tropospheric profiles on forecasts of radar reflectivity, as well as on thermodynamic, stability and wind profiles. Figure 10 shows the evolution of the convection event including the Multi-Radar Multi-Sensor (MRMS) radar reflectivity mosaic (Zhang et al. 2005; NOAA/National Severe Storms Laboratory 2019) and reflectivity forecasts initialized by the ensemble mean analysis of each DA experiment from

0500 UTC 14 June 2019. Radar observations show CI near the observing sites in northern Oklahoma and in southern Kansas at 0515 UTC on June 14 (Fig. 10a). We will refer to the CI in the south, centered at 36.9°N and 97.1°W, as S.C and the CI in the north that is centered at 37.9°N and 97.5°W as N.C (Fig. 10a). These locations are determined by the location of the new convective cells in the mosaic radar data. Both S.C and N.C grew, merged with convection approaching from the west and organized to form a squall line around 0800 UTC, which then moved eastward (Figs. 10b-d). In this study, we focused on the profiling observation impact on forecasting the initiation and early evolution of N.C and S.C. The CNTL experiment (Figs. 10e, f) predicted S.C east of and with stronger intensity than that in the radar observations (Figs. 10a, b). CNTL did not predict the development of N.C until after 0600 UTC (Figs. 10f, g, h), and the predicted convection over Kansas in N.C was weaker and east of that in the observations (cf. Figs. 10c, d with Figs. 10g, h).

CNTL_AERI showed overall similar forecasts to CNTL before 0700 UTC, indicating that the thermodynamic profiles of AERI has a negligible impact on the forecasts of the CI at N.C and S.C (Figs. 10i and j). During the entire forecast period, similar to CNTL, CNTL_AERI forecasted S.C. that was more than 10 dBZ stronger and biased eastward by 70 km, compared to observations of 30 dBZ (Figs. 10i-l). In contrast to the CNTL and CNTL_AERI experiments, assimilating MPD water vapor profiles was able to predict initiation of N.C in south-central Kansas by 0600 UTC (Fig. 10n), and it also partially mitigated the convection prediction shown by CNTL_AERI southeast of the S.C, leading to prediction of S.C's strength and structure closer to observation near the observation sites. However, after 0700 UTC CNTL_MPД predicted less organized S.C (Figs. 10o and p) compared to the observations (Figs. 10c and d), in contrast to CNTL and CNTL_AERI, which predicted a relatively stronger and eastward S.C above 50 dBZ. The ALL experiment showed a very similar forecast pattern to the CNTL_MPД (cf. Figs. 10m-o with Figs. 10q-s), but improved the forecast of N.C at 0800 UTC, forecasting convection that was more similar in location and intensity to observations than CNTL_MPД (Figs. 10p and t). Assimilating MPD profiles (CNTL_MPД and ALL) improved the location of CI and convection intensity forecasts compared to CNTL, but it still showed faster propagation of the linear convective bands compared to observations. This may be due to the limited horizontal coverage of MPD, AERI and

DWL, which restricts their ability to correct for forecast errors in the large-scale environment affecting the evolution and propagation of convective systems.

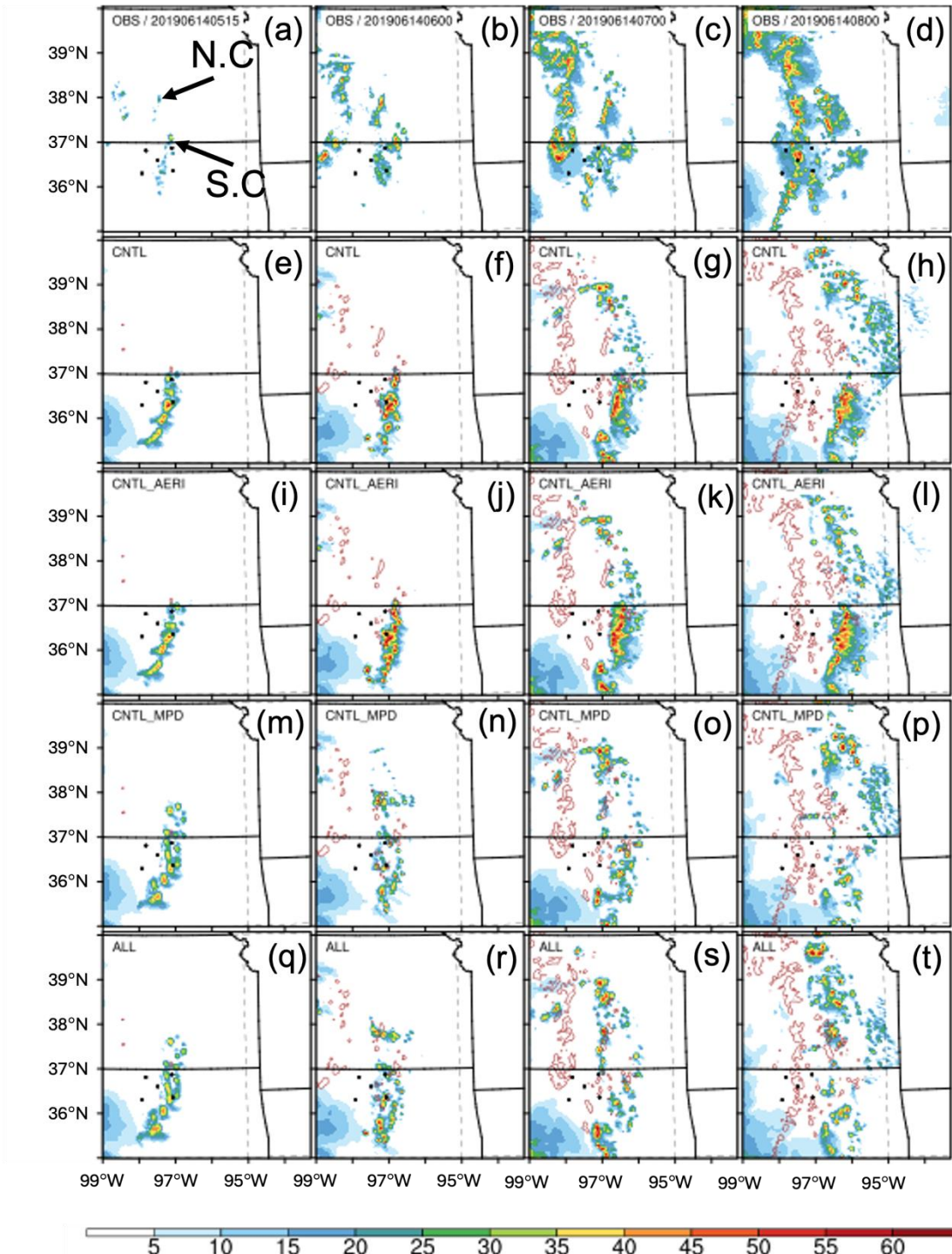


Figure 10. (a)-(d) Composite reflectivity (dBZ; color fill) of the convection event from 0515 UTC to 0800 UTC 14 June 2019 with radar observations and predictions of composite reflectivity for (e)-(h)

CNTL, (i)-(l) CNTL_AERI, (m)-(p) CNTL_MPД, and (q)-(t) ALL experiments initialized at 0500 UTC 14 June 2019. The overlaid solid red contours represent reflectivity of nature run greater than 30 dBZ. The reflectivity radar observations are provided by the Multi-Radar Multi-Sensor (MRMS) project (Zhang et al. 2005). The black dots indicate the location of profilers. The black arrows in (a) indicate the northern convection cells (N.C) and southern convection cells (S.C) of interest.

Figure 11 shows the Fractions Skill Scores (FSS) of the four DA experiments and one experiment with no DA computed against radar observations. The mosaic radar observations were interpolated to the 3-km D02 model grid shown in Fig. 6, and the FSS were computed for the domain area in Fig. 10. The paired *t* test adopting a significance level of 95% is used between ALL and other DA experiments. Each of the DA experiments, except for CNTL, showed an improvement in skill at most forecast times compared to when no observations were assimilated (NoDA). For a small FSS neighborhood of 48 km, CNTL_MPД showed the highest skill in the early hours up to 0630 UTC, which was approximately 0.05 higher than the next best, ALL, with statistical significance at 0615 UTC. CNTL_AERI, on the other hand, had the significantly lowest skill early in the forecast, comparable to CNTL, and then had a 0.07 higher skill than CNTL_MPД after 0700 UTC. ALL maintained a relatively high skill with statistical significance for most of the forecast time (with exception with CNTL_AERI after 0715 UTC), especially after 0630 UTC, when CNTL_MPД's skill decreased compared to CNTL_AERI. This is due to the relative improvement of N.C forecasts of ALL compared to CNTL_MPД. For a large neighborhood of 96 km, each DA experiment (Figure 11b) showed a similar FSS trend, although about 0.3 higher than those from the 48 km neighborhood results (Figure 11a), reflecting that each DA experiment has a similar location error of forecast. This result has been tested with forecasts of different initialization time from 0430 UTC to 0600 UTC with 15-minute intervals to increase verification sample size, and their averaged FSS was consistent with Fig. 11 (not shown).

The FSS trends (Fig. 11) are consistent with the qualitative results of the horizontal reflectivity forecasts in Fig. 10. The assimilation of MPД (CNTL_MPД and ALL) had the strongest positive impact for the first 1.5-hr forecast time, showing higher skill compared to CNTL_AERI. The MPД positive impact continued until 0630 UTC by better predicting the timing and location of the CI of both S.C and N.C. After 0700 UTC, however, CNTL_AERI and ALL showed the highest skill by forecasting a still eastward biased S.C, but with similar intensity of S.C to the observations despite its distance error. ALL showed higher skill than CNTL_MPД after 0700 UTC by improving the N.C forecast relative to CNTL_MPД.

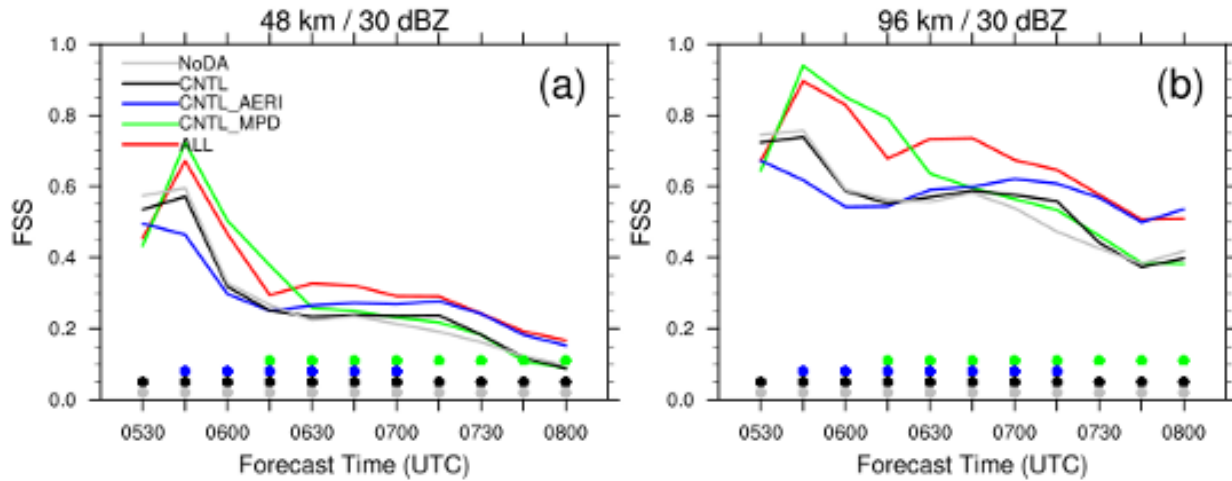


Figure 11. Fractions skill scores for the four DA experiments defined in Table 4 calculated with a (a) 48-km and (b) 96-km neighborhood for radar reflectivity >30 dBZ. The gray line represents the FSS of the experiment without assimilating observations (NoDA). The filled circle indicates that FSS differences between ALL and CNTL_MPD (green), ALL and CNTL_AERI (blue), and ALL and CNTL (black) are statistically significant at or above the 95 % confidence level by applying the paired t-test at the corresponding forecast time.

b. Detailed analysis

To investigate the profiling observation impact on the forecast for initiation and evolution of N.C and S.C, we examined the time series of convergence and vertical wind in the regions of N.C and S.C. Figure 12 shows a time-height cross-section of convergence and vertical wind averaged over 200 m vertical intervals and averaged over a 9 km horizontal radius centered on N.C and S.C in Fig. 10. The 9 km horizontal and 200 m vertical averaging result in a smoother representation of the field and allow for a more comparable resolution with observations. Figure 12 shows the DA analysis from 0300 UTC to 0500 UTC, continuing with the free forecast initialized at 0500 UTC. For the N.C, CNTL showed elevated convergence at about 1-2 km AGL during the DA period (0300 UTC to 0500 UTC) and the forecast period (0515 UTC to 0730 UTC), and divergence at 2-3 km AGL after 0415 UTC. This elevated convergence surmounted by divergence intensified after 0515 UTC consistent with the timing of the stage 4 1-hr accumulated precipitation data that started at 0515 UTC (Fig. 5a). The upward vertical motion was found from 0430 UTC to 0530 UTC above 2 km AGL, but no significant upward motion was forecast at 0600 UTC, inconsistent

with precipitation observations (Fig. 5a). CNTL_AERI shows a similar convergence/divergence pattern and updraft evolution as CNTL (Fig. 12b). CNTL_MPД shows relatively stronger convergence/divergence from 0515 to 0630 UTC compared to the previous two DA experiments, consistent with a stronger concurrent updraft maximum of 10 cm s^{-1} from ??0400??0515 UTC to 0630 UTC (Fig. 12c). Therefore, the assimilation of MPД enhanced the vertical velocity and improved the forecast of CI of the N.C, which can be confirmed in Figs. 10m, n and the FSS in Fig. 11. The ALL experiment (Fig. 12d) showed stronger convergence and divergence compared to CNTL_AERI (Fig. 12b) and after 0630 UTC compared to CNTL_MPД (Fig. 12c). This stronger convergence/divergence pattern after 0630 UTC led ALL to forecast stronger updrafts of 20 cm s^{-1} (Fig. 12d), resulting in stronger N.C convection (Fig. 10t).

It is noted that N.C is about 100 km from the northernmost observing sites, and the background was corrected by the correlation between the observations and the model background state at N.C. with the selected localization radius in this study. Therefore, the structure of the background error covariance estimated by the ensemble had important implications for the analysis and forecast of N.C. Assimilating MPД water vapor profiles partially affected the improvement in CI forecasts by changing the above surface wind analysis near N.C through background error correlation between the MPД water vapor profiles and the kinematic states during the DA cycling period, even far away from the observations.

The DA experiments showed a distinctly different low-level wind structure and evolution of the S.C compared to the N.C. In most DA experiments, S.C showed relatively weak elevated convergence at 2 km AGL and upper-level divergence during the DA period and forecast period compared to N.C. Near S.C, CNTL predicted weak elevated convergence and associated 5 cm s^{-1} upward motion between 0500 and 0530 UTC, whereas after 0545 UTC CNTL predicted stronger $10-15 \text{ cm s}^{-1}$ upward motion between 1-4 km AGL (Fig. 12e). CNTL_AERI had a similar but slightly stronger elevated convergence and corresponding upward motion from 0300 to 0530 UTC (Fig. 12f). CNTL_MPД (Fig. 12g) analyzed a weaker pattern of elevated convergence overlain by upper-level divergence than in CNTL and CNTL_AERI during the DA period, but it predicted a strong upward motion of about 20 cm s^{-1} from 0500 to 0515 UTC when the S.C was initiated (Fig. 12g). CNTL_MPД predicted more variable vertical motion with vertically deep

downdrafts between 0530 and 0600 UTC, followed by upward motion of 15 cm s^{-1} after 0600 UTC. ALL (Fig. 12h) showed similar analysis and forecasts to CNTL_MPД, but weaker upward motion compared to CNTL_MPД at 0515 UTC (Fig. 12h).

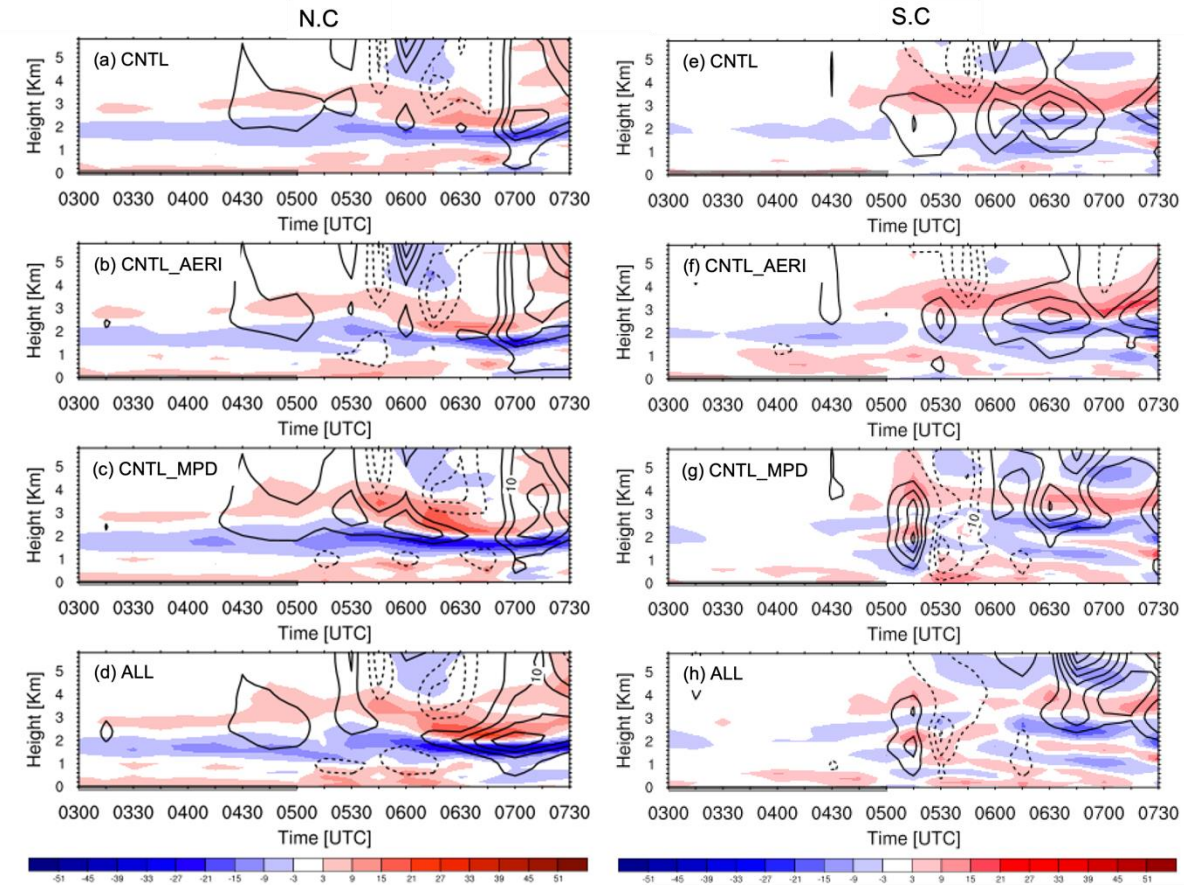


Figure 12. Time-height cross section for divergence (shaded in 6 s^{-1} intervals) and vertical wind (solid black lines for positive values and dotted black line for negative values with 5 cm s^{-1} intervals) from 0300 UTC 14 June to 0730 UTC June 2019 with 15-minute intervals for (a) CNTL, (b) CNTL_AERI, (c) CNTL_MPД and (d) ALL at the N.C site averaged over 9 km radius. The time-height cross sections of (a)-(d) are from the analysis from 0300 UTC 14 June to 0500 UTC 14 June and forecast initialized from 0500 UTC 14 June. (e)-(h) are the same as (a)-(d) but for the S.C site averaged over 9 km radius. The thick black segment on the x-axis indicates the DA period from 0300 UTC to 0500 UTC 14 June 2019.

To explore the evolution of thermodynamic fields, we examined time-height sections of convective available potential energy (CAPE) and time series of maximum convective inhibition

(MCIN) near N.C and S.C (Fig. 13). The CAPE was calculated by lifting parcels from each 200-m deep vertical level and averaged over a 9 km radius centered on N.C and S.C, and the MCIN was calculated only for the parcel at the height of the maximum equivalent potential temperature (Colman 1990). For the N.C, CNTL (Fig. 13a) and CNTL_AERI (Fig. 13b) had maximum CAPE values that were less than 1200 J kg^{-1} in the analysis and forecast period. In contrast, CNTL_MP (Fig. 13c) and ALL (Fig. 13d) had a larger maximum CAPE of $\sim 1500 \text{ J kg}^{-1}$ analyzed and forecasted around 2 km AGL. In particular, ALL predicted stronger convergence between 1-2 km and divergence above that (Fig. 12d), which can maintain a more advantageous lifting environment compared to CNTL_MP (Fig. 13d). This favorable lifting environment, along with the forecast of larger maximum CAPE values above 2 km AGL (Fig. 13d), explains that ALL was more likely to predict strong convection compared to CNTL_MP. The MCIN values were smaller than 50 J kg^{-1} for all DA experiments, with CNTL_MP and ALL having less MCIN than CNTL and CNTL_AERI during most of the DA and forecast periods, possibly increasing the convective development. For S.C, all experiments showed smaller CAPE in the analysis and forecasts compared to N.C. From 0500 UTC to 0700 UTC in the S.C region (Figs. 10a-c), CNTL_MP and ALL (Figs. 13g, h) predicted smaller CAPE that was confined to narrower vertical ranges than for CNTL and CNTL_AERI (Figs. 13e, f). It is noted that all DA experiments predicted MCIN less than 10 J kg^{-1} during the DA periods perhaps allowing the small convective potential to be fully realized (Figs. 13e-h).

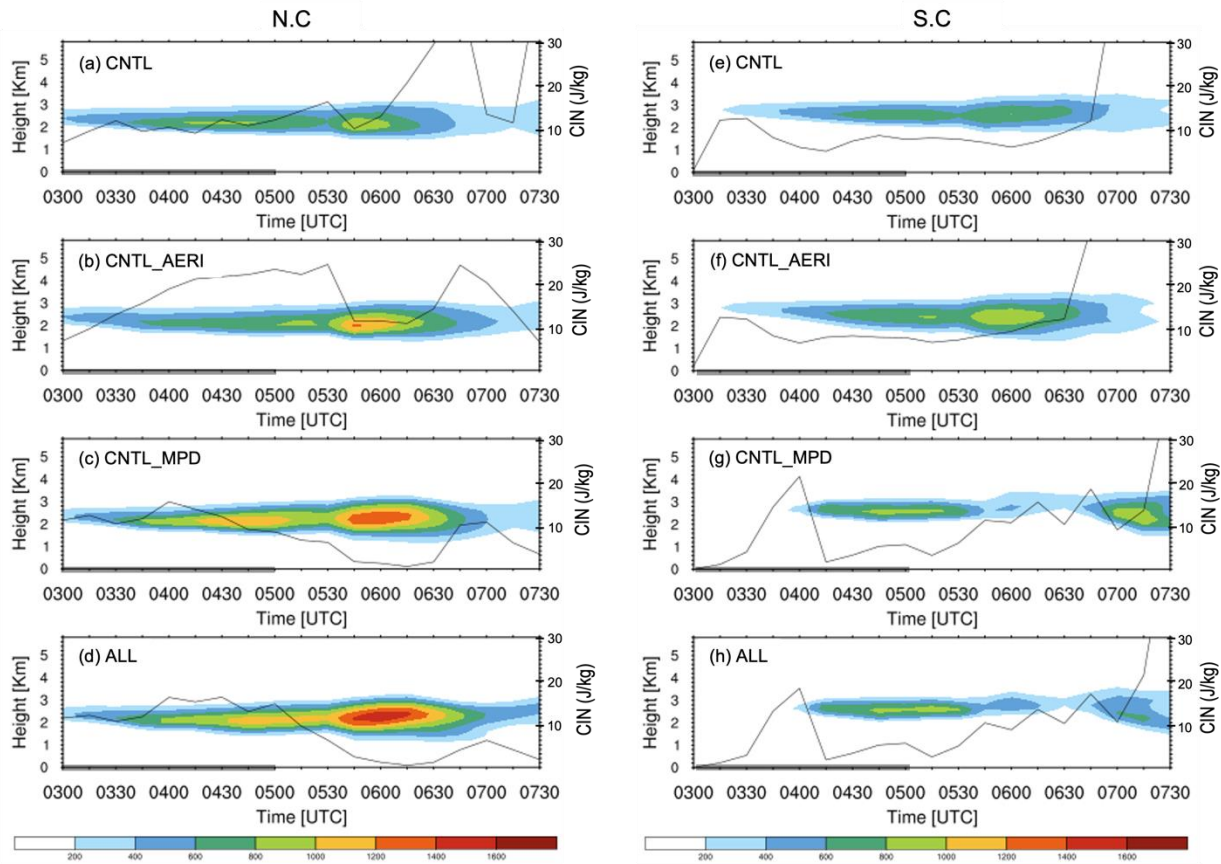


Figure 13. Time-height cross section for CAPE (shaded in 200 J kg^{-1} intervals) and time series of MCIN (contoured) from 0300 UTC to 0730 UTC 14 June 2019 with 15-minute intervals for (a) CNTL, (b) CNTL_AERI, (c) CNTL_MPD and (d) ALL averaged over a 9-km radius centered on N.C shown in Fig. 10a. (a)-(d) are from the analysis from 0300 UTC 14 June to 0500 UTC 14 June and forecast initialized from 0500 UTC 14 June. (e)-(h) are the same as (a)-(d) but for the S.C site averaged over 9 km radius. The thick black segment on the x-axis indicates the DA period from 0300 UTC to 0500 UTC 14 June 2019.

Compared to the S.C, the N.C had larger CAPE at most DA and forecast periods. To explore the impact of assimilating each profiler on N.C, we examined the vertical profiles of the T and Q analysis at 0500 UTC, the last DA cycle (Fig. 14). For N.C, CNTL had less water vapor at most vertical levels compared to the other three DA experiments and assimilating AERI or MPD increased water vapor relative to CNTL (Fig. 14a). Assimilating MPD increased the water vapor analysis by $\sim 1\text{-}2 \text{ g kg}^{-1}$ compared to CNTL_AERI, especially below 600 m AGL and between 2 and 3 km AGL. ALL produced the greatest amount of water vapor throughout the profile below 2.2 km AGL in the final analysis time (Fig. 14a). The lowest useful range of MPD profiles during this project is 700 m AGL, and it is shown that assimilating MPD water vapor profiles can

effectively spread their influence below the lowest useful range of MPD of 700 m AGL through the estimated vertical correlation between MPD profiling data and the modeled thermodynamic state near the surface given the selected localization radius in this study. Assimilating AERI thermodynamic profiles resulted in a similar vertical temperature structure to ALL, and their profiles were about 1 to 2 K cooler than the other two experiments below 1.6 km AGL (Fig. 14b). CNTL_AERI showed an increase in equivalent potential temperature from the surface to 2 km AGL, except for around 0.4 km AGL, compared to CNTL (Fig. 14c). CNTL_MPД and ALL analyzed equivalent potential temperature that were about 4-5 K higher than the other two experiments from the surface to 0.8 km AGL, and 1-2 K higher up to 3 km AGL (Fig. 14c).

For S. C. (Fig. 14d), CNTL_AERI was the only experiment that lacked a dry layer 600 m – 2.4 km AGL. Assimilating MPD (i.e., CNTL_MPД and ALL) increased water vapor below 500 m and decreased it above 700 m compared to CNTL_AERI and CNTL (Fig. 14d). The temperature profile from ALL was closer to CNTL_AERI than CNTL_MPД below 1.8 km AGL due to the influence of assimilating AERI temperature profiles (Fig. 14e), but ALL had a similar vertical water vapor structure to CNTL_MPД (Fig. 14d). The temperature analysis at S.C had a more pronounced mixed layer than near N.C, with a stronger temperature inversion starting at ~600 m, especially for ALL and CNTL_MPД (Fig. 14e). Assimilating AERI (CNTL_AERI and ALL) produced a cooler profile by about 1-2 K below 1.8 km (Fig. 14e) than those that did not assimilate AERI (CNTL and CNTL_MPД). CNTL_MPД and ALL showed decreasing equivalent potential temperature, indicating potential instability between 0.4 km and 0.8 km AGL, and all DA experiments showed potential instability above 2.5 km (Fig. 14f).

The experiments that assimilated MPD (CNTL_MPД and ALL) had increased water vapor near 600 m AGL and above 2 km AGL for N.C compared to the other two experiments, especially when compared to CNTL_AERI (Fig. 14a), and this difference in water vapor analysis led to a larger CAPE above 2 km for N.C during the DA cycle. In contrast, due to less water vapor near ~ 1 km AGL, the S.C had relatively smaller maximum CAPE than for N.C. However, as for N.C, maximum CAPE in the vertical profiles (Fig. 13e-h) are more strongly influenced by water vapor differences than by temperature differences.

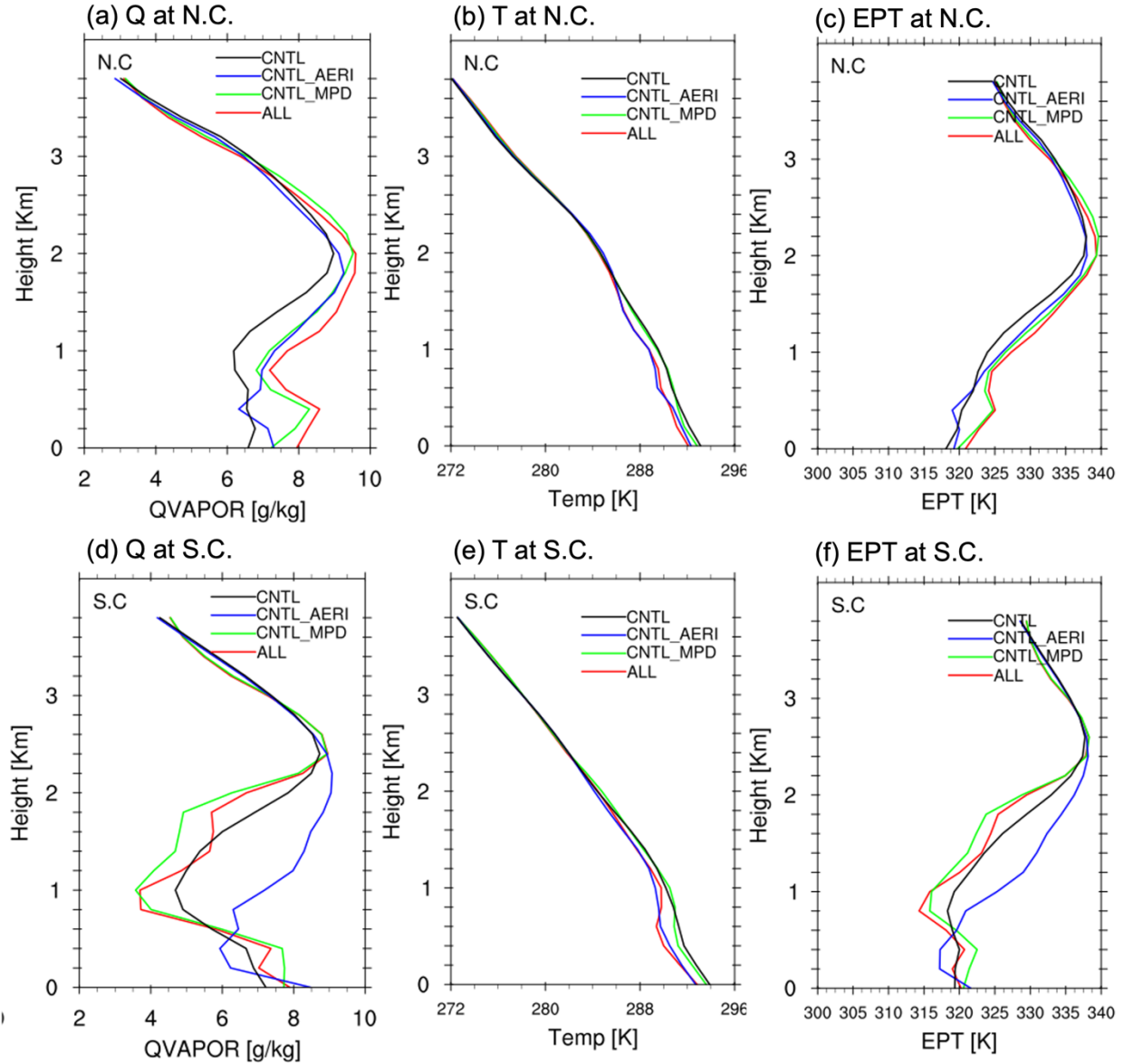


Figure 14. Vertical profiles of (a) water vapor mixing ratio (g kg^{-1}), (b) temperature (K) and (c) equivalent potential temperature (K) analysis at N.C at 0500 UTC 14 June 2019. (d)-(f) are the same as (a)-(c) but at S.C.

Figure 15 shows a time-height cross-section of water vapor mixing ratio, equivalent potential temperature, and cloud water mixing ratio for N.C and S.C. For N.C, each experiment simulated an elevated moist layer at about 1-3 km AGL during the DA and forecast periods (Figs. 15a-d). CNTL and CNTL_AERI simulated a localized cloud mixing ratio of about 0.5 g kg^{-1} at 2.5-3.5

km AGL from 0445 to 0515 UTC, implying saturation at the localized layers for about 30 minutes (Figs. 15a-b). However, CNTL and CNTL_AERI simulated maximum CAPE less than 800 J kg^{-1} during this time at about 2 km AGL (Figs. 13a-b) and no significant upward motion at the DA period and early forecast time (Figs. 12a-b), therefore these two experiments did not forecast CI at N.C (Figs. 15a-b). Compared to CNTL and CNTL_AERI, CNTL_MPД showed a more rapid increase in the water vapor analysis at 2 km AGL during the DA period, reaching 9 g kg^{-1} at 0500 UTC (Fig. 15c). This increasing elevated moisture led to greater thermodynamic instability with maximum CAPE values $\geq 1400 \text{ J kg}^{-1}$ from 0500 to 0600 UTC (Fig. 13c) compared to ~ 1000 - 1200 J kg^{-1} for CNTL and CNTL_AERI (Figs. 13a,b). CNTL_MPД also simulated elevated convergence consistent with upward motion during 0430 to 0630 UTC (Fig. 12c), and forecasted cloud water mixing ratio at 2 km AGL after 0530 UTC (Fig. 15c). These conditions contributed to forecasted reflectivity above 30 dBZ after 0530 UTC, which is consistent with the CI observations of N.C (Fig. 10a).

For N.C, DA experiments simulated thermodynamic instability and elevated convergence, which likely contributed to the CI. In particular, the assimilation of MPD improved the forecast of N.C by increasing the entire profile of water vapor content below 3 km and by enhancing elevated convergence between 1 - 2 km to induce vertical lifting and through improved analysis of the features of these thermodynamic and kinematic fields during the DA period. In contrast, the S.C was characterized by less thermodynamic instability and less structured vertical convergence and divergence compared to the N.C. Under those less favorable conditions for initiating convection, the CNTL_MPД and ALL experiments produced CI that is more consistent with the observations in the early forecasts around 0515 UTC (Figs. 12g and h), while CNTL and CNTL_AERI simulated elongated convective bands that were stronger, more organized, and moved more rapidly than observed (Fig. 10). Thus, CI and evolution of S.C might be governed by different mechanisms than in N.C. In particular, assimilation of MPD water vapor profiles reduced the intensity of simulated convection and its eastward location bias compared to CNTL. Unlike for N.C, S.C cells are located close to or within the radius of influence of the profiling observations, so model state variables were more adjusted by assimilating MPD water vapor profiling observations. Taking this into account, we examined how changes in water vapor due to MPD assimilation improved the forecast of S.C.

For S.C, CNTL produced a deep elevated moist layer from 1.5 km to 3 km AGL and analyzed a saturated state above 2 km AGL during the DA period. However, CNTL became unsaturated with a decreasing cloud water mixing ratio in the early forecast time. CNTL_AERI provided similar analysis to CNTL during the DA period, but with a deeper elevated moist layer from 1 to 3 km AGL during the DA and forecast period compared to CNTL. However, the analysis and forecasts of CNTL_AERI had small CAPE values that were less than 800 J Kg^{-1} (Fig. 13f). Compared to CNTL_AERI, CNTL_MP and ALL were moister from the surface to 0.5 km AGL and then drier up to about 2 km, with a relatively thin elevated moist layer located at about 2-3 km AGL (Fig. 15g, h).

All DA experiments simulated a saturated layer at 2.5-3 km AGL from 0415 UTC to 0515 UTC during the DA and early forecast period, and predicted the decreasing equivalent potential temperature above 2.5 km indicating a potential instability layer during the DA and forecast periods (Figs. 15e-h). In all DA experiments, the superposition of a saturated layer with a potential instability layer suggests that an elevated moist absolutely unstable layer (MAUL; Bryan and Fritsch 2000; Trier et al. 2017) existed above 2.5 km AGL at 0500 UTC when CI was observed (Figs. 15e-h). Under these conditions of S.C, CNTL and CNTL_AERI simulated a more intense, more organized, and eastward-biased elongated convective band than observations. In contrast, CNTL_MP and ALL predicted CI that was more consistent with the observed timing, location and intensity (Fig 10). This is likely because the assimilation of MPD improved the analysis of CNTL_MP and ALL with dry air in the lower layers below 2.5 km (Figs. 14e-f and 15e-f), thereby suppressing convective activity. The presence of dry air in the lower layers of CNTL_MP and ALL can limit the supply of water vapor required for deep convection, thereby playing a role in preventing the overprediction of convection seen in the other two experiments (Fig. 10). The vertical structure of low-level water vapor in CNTL_MP and ALL forecasts aligns more closely with the radiosonde observations at 0600 UTC at C1 than that of the other two experiments (not shown).

Assimilating MPD (CNTL_MP and ALL) improved CI forecasts in N.C by simulating larger elevated conditional instability and an environment of convergence and associated ascent.

Assimilation of MPD improved CI forecasts within MAUL conditions of S.C by improving the water vapor profile and mitigating the development of spurious convection that were forecast in CNTL and CNTL_AERI..

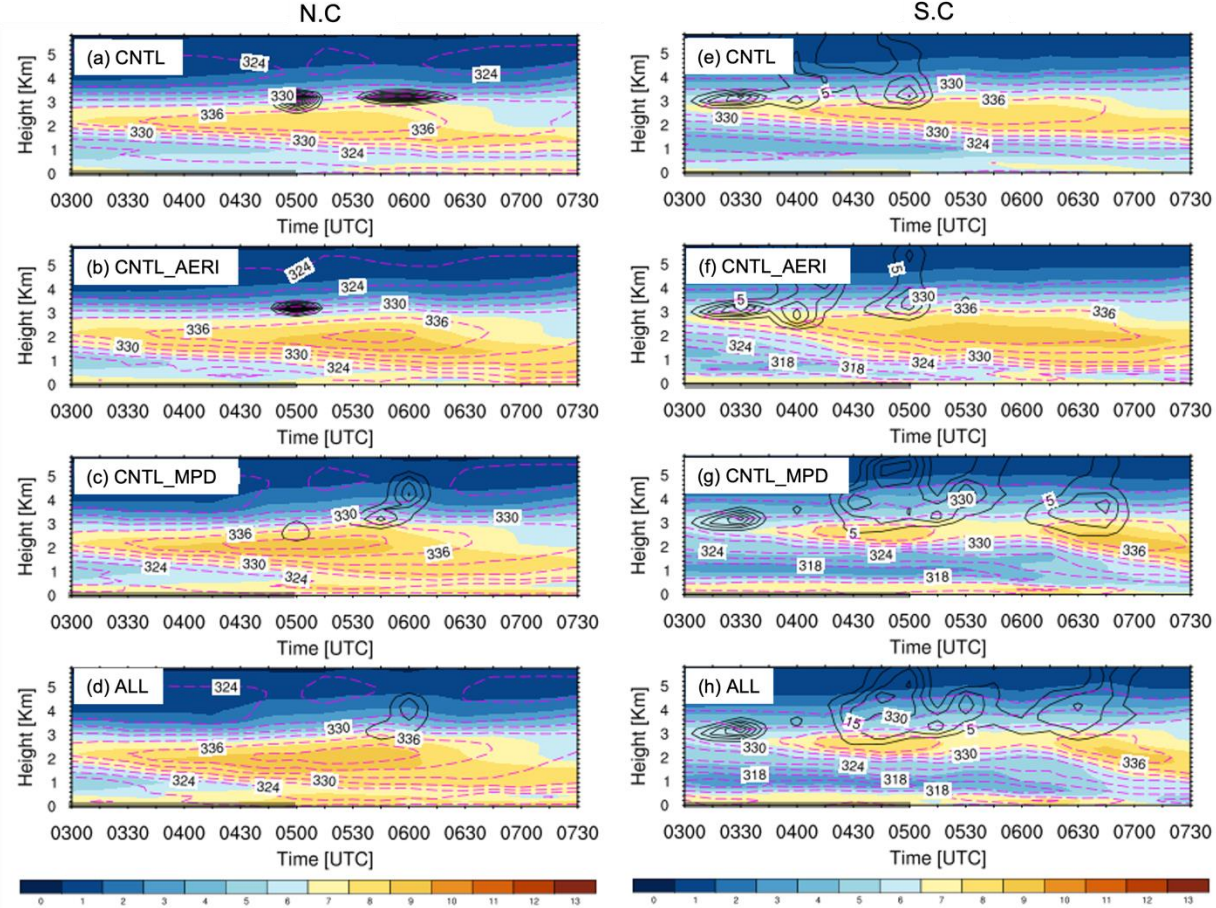


Figure 15. Time-height cross section for water vapor mixing ratio (shaded in $1\ g\ kg^{-1}$ intervals), equivalent potential temperature (contoured in dashed magenta lines at $2\ K$ intervals), and cloud water mixing ratio ($0.05\ g\ kg^{-1}$ contours in black) from 0300 to 0730 UTC 14 June 2019 with 15-minute intervals for (a) CNTL, (b) CNTL_AERI, (c) CNTL_MP and (d) ALL at the N.C site averaged over 9 km radius. The time-height cross sections of (a)-(d) are from the analysis from 0300 to 0500 UTC 14 June and forecast initialized from 0500 UTC 14 June. (e)-(h) are the same as (a)-(d) but for at the S.C site averaged over 9 km radius. The thick black segment on the x-axis indicates the DA period from 0300 UTC to 0500 UTC 14 June 2019.

6. Summary and discussion

The MPD Network Demonstration Project was conducted from April to July 2019 to deploy five MPDs that were collocated with the DOE/ARM/SGP observatory instruments including AERIs

and DWLs near Lamont, Oklahoma. This field campaign was designed to investigate the effect of MPD, a new water vapor profiler developed jointly by NCAR and MSU, in complementing the other ground-based remote sensing profilers on improving severe weather prediction skill. MPD has been shown to substantially improve precipitation prediction within the OSSE framework (Kay et al. 2022). This study is the first to explore the effect of assimilating actual MPD profiles on convective weather prediction. In this study, a precipitation case characterized by nocturnal CI and subsequent linear convective organization over Oklahoma on 14 June 2019 is analyzed. Since this case had accurate forecasted winds, the impact of DWL assimilation was negligible, allowing us to focus on the impact of the thermodynamic profiles of AERI and MPD. We conducted four DA experiments. The experiment assimilating conventional observations and DWL was used as the control DA experiment (CNTL), followed by experiments assimilating each of the AERI and MPD thermodynamic profilers (CNTL_AERI and CNTL_MP) and an experiment assimilating all profilers together (ALL).

The effect of each profiler observation was examined for the northern CI (N.C) observed in Kansas and the southern CI (S.C) observed in northern Oklahoma. For N.C, AERI did not show a significant effect on the prediction of location and intensity of the CI compared to CNTL. This is likely due to the coarse vertical resolution and short vertical range of the AERI moisture profile limiting its impact on CIs farther away from the observing sites. Assimilation of MPD, on the other hand, improved the N.C forecasts, and this improvement is mainly attributed to two causes: 1) MPD increased the amount of low-level water vapor, which increased thermodynamic instability; and 2) Assimilation of MPD enhanced the low-level convergence in southern Kansas where the DWL and AERI profiles had little impact, leading to a simulated environment of significant ascent that aided CI. These changes in the dynamical and thermodynamic pre-convective environment by assimilating MPD water vapor profiles improved the prediction of the location and timing of new convection.

The mechanism for CI in S.C is apparently different than for N.C. In particular, similar to N.C., the experiments simulated a pattern of elevated convergence and divergence at S.C., but with relatively weaker intensity. Assimilating MPD water vapor profiles modified the analysis of the vertical structure of water vapor of a dry layer centered around 1 km and a moist layer above

compared to CNTL_AERI. The MPD water vapor assimilation resulted in an improvement of the location, structure and intensity of the convective system. Along with the MAUL conditions, MPD effectively adjusted the vertical thermodynamic structure of the lower layer, mitigating the stronger convection simulated in CNTL_AERI and predicting convection initiation and evolution more consistent with observations. Assimilating both AERI and MPD profiles (ALL) was similar to the results of assimilating MPD alone in the analysis and subsequent forecast, with a slight improvement in reflectivity prediction skill. This is because most of the improvement was contributed by assimilating MPD water vapor profiles. Despite these improvements, the forecasts from all DA experiments still show the elongated convective band moving eastward faster than the observations, which can be attributed to model biases of physics parameterizations and model resolution. In addition, assimilation of the limited profiler network is not able to fully resolve the detailed features of the precipitation system.

This study is the first to illustrate the observation impact of assimilating observed MPD water vapor profiles and shows a significant positive effect of MPD on a selected precipitation event. Water vapor at 1-3 km altitude is an important factor in the initiation and development of convective weather systems. The results of this study, although based on a single case study, suggest that continuous water vapor profiles from MPD can significantly contribute to improving model-based convective weather forecasts. In the future, we plan to explore the systematic impact of MPD water vapor profiles on various severe weather conditions by using the MPD and other profilers. We will also develop more advanced methods to estimate the observation error of MPD and apply them to future data assimilation studies. In addition, we plan to explore the effect of model biases and the effect of multiscale DA on profiler assimilation in the future.

Acknowledgments

This material is based upon work supported by the NSF National Center for Atmospheric Research (NCAR), which is a major facility sponsored by the National Science Foundation under Cooperative Agreement No. 1852977. We acknowledge the high-performance computing support from Cheyenne (doi:10.5065/D6RX99HX) provided by the Computational and Information Systems Laboratory (CISL) at the NSF NCAR and sponsored by the NSF. Support from the NCAR Short-Term Explicit Prediction (STEP) program and NOAA Award Nos.

NA19OAR4590320 and NA23OAR4590399 are gratefully acknowledged. We thank Jenny Sun, Matthew Hayman and Stan Trier for comments that greatly improved earlier versions of this manuscript. We are grateful to three anonymous reviewers for thorough reviews that substantially improved the clarity of this manuscript.

Data availability statement. Computing and data storage resources, including the Cheyenne supercomputer (<https://doi.org/10.5065/D6RX99HX>), were provided by the Computational and Information Systems Laboratory (CISL) at NCAR. The raw model/reanalysis data including NCEP GFS, FNL, and conventional observed data can be downloaded online at UCAR Research Data Archive (RDA) datasets (<https://rda.ucar.edu/>). The MPD data can be downloaded online from <https://data.eol.ucar.edu/dataset/597.001>. The DWL and AERI data can be downloaded online through following link: <http://dx.doi.org/10.5439/1178583> and <http://dx.doi.org/10.5439/1483830>, respectively.

References

- Aitken, M. L., M. E. Rhodes, and J. K. Lundquist, 2012: Performance of a Wind-Profilin Lidar in the Region of Wind Turbine Rotor Disks. *J. Atmos. Oceanic Technol.*, **29**, 347–355, <https://doi.org/10.1175/JTECH-D-11-00033.1>.
- Anderson, J. L., T. Hoar, K. Raeder, H. Liu, N. Collins, R. Torn, and A. Avellano, 2009: The Data Assimilation Research Testbed: A community facility. *Bull. Amer. Meteor. Soc.*, **90**, 1283–1296, <https://doi.org/10.1175/2009BAMS2618.1>.
- Atmospheric Radiation Measurement (ARM) user facility. 2010. Doppler Lidar Horizontal Wind Profiles (DLPROFWIND4NEWS). 2010-11-02 to 2023-07-10, Southern Great Plains (SGP) Central Facility, Lamont, OK (C1). Compiled by T. Shippert, R. Newsom and L. Riihimaki. ARM Data Center. Data set accessed 2023-07-12 at <http://dx.doi.org/10.5439/1178582>.
- Atmospheric Radiation Measurement (ARM) user facility. 2016. AERIoe Thermodynamic Profile and Cloud Retrieval (AERIOE1TURN). 2016-01-01 to 2023-06-13, Southern

Great Plains (SGP) Central Facility, Lamont, OK (C1). Compiled by T. Shippert. ARM Data Center. Data set accessed at <http://dx.doi.org/10.5439/1483830>.

Barker, D. M., W. Huang, Y.-R. Guo, A. J. Bourgeois, and Q. N. Xio, 2004: A three-dimensional variational data assimilation system for MM5: Implementation and initial results. *Mon. Wea. Rev.*, **132**, 897–914, [https://doi.org/10.1175/1520-0493\(2004\)132<0897:ATVDAS>2.0.CO;2](https://doi.org/10.1175/1520-0493(2004)132<0897:ATVDAS>2.0.CO;2).

Browning, K. A., and R. Wexler, 1968: The Determination of Kinematic Properties of a Wind Field Using Doppler Radar. *J. Appl. Meteor. Climatol.*, **7**, 105–113, [https://doi.org/10.1175/1520-0450\(1968\)007<0105:TOKPO>2.0.CO;2](https://doi.org/10.1175/1520-0450(1968)007<0105:TOKPO>2.0.CO;2).

Bryan, G. H., and J. M. Fritsch, 2000: Moist Absolute Instability: The Sixth Static Stability State. *Bull. Amer. Meteor. Soc.*, **81**, 1207–1230, [https://doi.org/10.1175/1520-0477\(2000\)081<1287:MAITSS>2.3.CO;2](https://doi.org/10.1175/1520-0477(2000)081<1287:MAITSS>2.3.CO;2).

Chan, S.C., E. J. Kendon, H. J. Fowler, 2023: Large-scale dynamics moderate impact-relevant changes to organised convective storms. *Commun. Earth Environ.* **4**, 8. <https://doi.org/10.1038/s43247-022-00669-2>.

Chen, F., and J. Dudhia, 2001: Coupling an advanced land surface–hydrology model with the Penn State–NCAR MM5 modeling system. Part I: Model implementation and sensitivity. *Mon. Wea. Rev.*, **129**, 569–585, [https://doi.org/10.1175/1520-0493\(2001\)129<0569:CAALSH>2.0.CO;2](https://doi.org/10.1175/1520-0493(2001)129<0569:CAALSH>2.0.CO;2).

Chipilski, H. G., X. Wang, and D. B. Parsons, 2020: Impact of assimilating PECAN profilers on the prediction of bore-driven nocturnal convection: A multiscale forecast evaluation for the 6 July 2015 case study. *Mon. Wea. Rev.*, **148**, 1147–1175, <https://doi.org/10.1175/MWR-D-19-0171.1>.

Chipilski, H. G., X. Wang, D. B. Parsons, A. Johnson, and S. K. Degelia, 2022: The value of assimilating different ground-based profiling networks on the forecasts of bore-generating nocturnal convection. *Mon. Wea. Rev.*, **150**, 1273–1292, <https://doi.org/10.1175/MWR-D-21-0193.1>.

Colman, B. R., 1990: Thunderstorms above frontal surfaces in environments without positive CAPE. Part I: A climatology. *Mon. Wea. Rev.*, **118**, 1103–1121.

Coniglio, M. C., J. Correia Jr., P. T. Marsh, and F. Kong, 2013: Verification of convection-allowing WRF model forecasts of the planetary boundary layer using sounding

observations. *Wea. Forecasting*, **28**, 842–862, <https://doi.org/10.1175/WAF-D-12-00103.1>.

Coniglio, M. C., G. S. Romine, D. D. Turner, and R. D. Torn, 2019: Impacts of targeted AERI and Doppler Lidar wind retrievals on short-term forecasts of the initiation and early evolution of thunderstorms. *Mon. Wea. Rev.*, **147**, 1149–1170, <https://doi.org/10.1175/MWR-D-18-0351.1>.

Craven, J. P., and H. E. Brooks, 2004: Baseline climatology of sounding derived parameters associated with deep moist convection. *Natl. Wea. Dig.*, **28**, 13–24. [Available online at http://www.nssl.noaa.gov/users/brooks/public_html/papers/cravenbrooks_nwa.pdf.]

Crook, N. A., 1996: Sensitivity of moist convection forced by boundary layer processes to low-level thermodynamic fields. *Mon. Wea. Rev.*, **124**, 1767–1785, [https://doi.org/10.1175/1520-0493\(1996\)124<1767:SOMCFB>2.0.CO;2](https://doi.org/10.1175/1520-0493(1996)124<1767:SOMCFB>2.0.CO;2).

Degelia, S. K., X. Wang, and D. J. Stensrud, 2019: An evaluation of the impact of assimilating AERI retrievals, kinematic profilers, rawinsondes, and surface observations on a forecast of a nocturnal convection initiation event during the PECAN field campaign. *Mon. Wea. Rev.*, **147**, 2739–2764, <https://doi.org/10.1175/MWR-D-18-0423.1>.

Degelia, S. K., X. Wang, D. J. Stensrud, and D. D. Turner, 2020: Systematic evaluation of the impact of assimilating a network of ground-based remote sensing profilers for forecasts of nocturnal convection initiation during PECAN. *Mon. Wea. Rev.*, **148**, 4703–4728, <https://doi.org/10.1175/MWR-D-20-0118.1>.

Desroziers, G., L. Berre, B. Chapnik, and P. Poli, 2005: Diagnosis of observation, background and analysis-error statistics in observation space. *Quart. J. Roy. Meteor. Soc.*, **131**, 3385–3396, <https://doi.org/10.1256/qj.05.108>.

Dierer, S., and Coauthors, 2009: Deficiencies in quantitative precipitation forecasts: Sensitivity studies using the COSMO model. *Meteor. Z.*, **18**, 631–645, <https://doi.org/10.1127/0941-2948/2009/0420>.

Ducrocq, V., D. Ricard, J. P. Lafore, and F. Orain, 2002: Storm-scale numerical rainfall prediction for five precipitating events over France: On the importance of the initial humidity field. *Wea. Forecasting*, **17**, 1236–1256, [https://doi.org/10.1175/1520-0434\(2002\)017<1236:SSNRPF>2.0.CO;2](https://doi.org/10.1175/1520-0434(2002)017<1236:SSNRPF>2.0.CO;2).

- Gaspari, G., and S. E. Cohn, 1999: Construction of correlation functions in two and three dimensions. *Quart. J. Roy. Meteor. Soc.*, **125**, 723–757, <https://doi.org/10.1002/qj.49712555417>.
- Geer, A. J., and P. Bauer, 2011: Observation errors in all-sky data assimilation. *Quart. J. Roy. Meteor. Soc.*, **137**, 2024–2037, <https://doi.org/10.1002/qj.830>.
- Geerts, B., and Coauthors, 2017: The 2015 Plains Elevated Convection At Night Field Project. *Bull. Amer. Meteor. Soc.*, **98**, 767–786, <https://doi.org/10.1175/BAMS-D-15-00257.1>.
- Hanesiak, J., and D. D. Turner, 2016: FP3 University of Manitoba Doppler Lidar wind profile data (version 1.0). UCAR/NCAR Earth Observing Laboratory, accessed 14 March 2018, <https://doi.org/10.5065/D60863P5>.
- Holley, D. M., S. R. Dorling, C. J. Steele, and N. Earl, 2014: A climatology of convective available potential energy in Great Britain. *Int. J. Climatol.*, **34**, 3811–3824, <https://doi.org/10.1002/joc.3976>.
- Hollingsworth, A. and P. Lönnberg, 1986: The statistical structure of short-range forecast errors as determined from radiosonde data. Part I: The wind field. *Tellus*, **38A**, 111–136.
- Hu, M., G. Ge, C. Zhou, D. Stark, H. Shao, K. Newman, J. Beck, and X. Zhang, 2018: Grid-point Statistical Interpolation (GSI) user's guide version 3.7. Developmental Testbed Center, 149 pp., <http://www.dtcenter.org/com-GSI/users/docs/index.php>.
- Hu, J., N. Yussouf, D. D. Turner, T. A. Jones, and X. Wang, 2019: Impact of ground-based remote sensing boundary layer observations on short-term probabilistic forecasts of a tornadic supercell event. *Wea. Forecasting*, **34**, 1453–1476, <https://doi.org/10.1175/WAF-D-18-0200.1>.
- Hu, G., S. L. Dance, R. N. Bannister, H. Chipilski, O. Guillet, B. Macpherson, M. Weissmann and N. Yussouf, 2023: Progress, challenges, and future steps in data assimilation for convection-permitting numerical weather prediction: Report on the virtual meeting held on 10 and 12 November 2021. *Atmos. Sci. Lett.*, **24**, e1130, <https://doi.org/10.1002/asl.1130>.
- Iacono, M. J., J. S. Delamere, E. J. Mlawer, M. W. Shephard, S. A. Clough, and W. D. Collins, 2008: Radiative forcing by long-lived greenhouse gases: Calculations with the AER

radiative transfer models. *J. Geophys. Res.*, **113**, D13103,
<https://doi.org/10.1029/2008JD009944>.

Ingleby, B., Rodwell, M., & Isaksen, L. (2016). Global radiosonde network under pressure. *ECMWF newsletter*, **149**, 25–30. <https://doi.org/10.21957/cblxtg> Available from <http://www.ecmwf.int/en/about/media-centre/media-resources>

James, E. P., and S. G. Benjamin, 2017: Observation system experiments with the hourly updating Rapid Refresh model using GSI hybrid ensemble-variational data assimilation. *Mon. Wea. Rev.*, **145**, 2897–2918. <https://doi.org/10.1175/MWR-D-16-0398.1>.

Janjić, Z. I., 2002: Nonsingular implementation of the Mellor–Yamada level 2.5 scheme in the NCEP Meso model. NCEP Office Note 437, 61 pp., <http://www.emc.ncep.noaa.gov/officenotes/newernotes/on437.pdf>.

Janjić, T., and Coauthors, 2017: On the representation error in data assimilation. *Quart. J. Roy. Meteor. Soc.*, **144**, 1257–1278, <https://doi.org/10.1002/qj.3130>.

Johns, R. H., and C. A. Doswell, 1992: Severe local storms forecasting. *Wea. Forecasting*, **7**, 588–612, [https://doi.org/10.1175/1520-0434\(1992\)007<0588:SLSF>2.0.CO;2](https://doi.org/10.1175/1520-0434(1992)007<0588:SLSF>2.0.CO;2).

Johnson, A., X. Wang, J. R. Carley, L. J. Wicker, and C. Karstens, 2015: A comparison of multiscale GSI-based EnKF and 3DVar data assimilation using radar and conventional observations for midlatitude convective-scale precipitation forecasts. *Mon. Wea. Rev.*, **143**, 3087–3108, <https://doi.org/10.1175/MWR-D-14-00345.1>.

Jones, T. A., K. Knopfmeier, D. Wheatley, G. Creager, P. Minnis, and R. Palikonda, 2016: Storm-scale data assimilation and ensemble forecasting with the NSSL experimental Warn-on-Forecast system. Part II: Combined radar and satellite data experiments. *Wea. Forecasting*, **31**, 297–327, <https://doi.org/10.1175/WAF-D-15-0107.1>.

Kain, J. S., 2004: The Kain–Fritsch convective parameterization: An update. *J. Appl. Meteor. Climatol.*, **43**, 170–181, [https://doi.org/10.1175/1520-0450\(2004\)043<0170:TKCPAU>2.0.CO;2](https://doi.org/10.1175/1520-0450(2004)043<0170:TKCPAU>2.0.CO;2).

Kain, J. S., and J. M. Fritsch, 1990: A one-dimensional entraining/detraining plume model and its application in convective parameterization. *J. Atmos. Sci.*, **47**, 2784–2802, [https://doi.org/10.1175/1520-0469\(1990\)047<2784:AODEPM>2.0.CO;2](https://doi.org/10.1175/1520-0469(1990)047<2784:AODEPM>2.0.CO;2).

- Kain, J. S., and J. M. Fritsch, 1993: Convective parameterization for mesoscale models: The Kain–Fritsch scheme. *The Representation of Cumulus Convection in Numerical Models*, Meteor. Monogr., No. 24, Amer. Meteor. Soc., 165–170
- Kay, J., T. M. Weckwerth, W. Lee, J. Sun, and G. Romine, 2022: An OSSE study of the impact of MicroPulse Differential absorption lidar (MPD) water vapor profiles on convective weather forecasting. *Mon. Wea. Rev.*, **150**, 2787–2811, <https://doi.org/10.1175/MWR-D-21-0284.1>.
- Keil, C., A. Röpnack, G. C. Craig, and U. Schumann, 2008: Sensitivity of quantitative precipitation forecast to height dependent changes in humidity. *Geophys. Res. Lett.*, **35**, L09812, <https://doi.org/10.1029/2008GL033657>.
- Kerr, C. A., D. J. Stensrud, and X. Wang, 2019: Diagnosing convective dependencies on near-storm environments using ensemble sensitivity analyses. *Mon. Wea. Rev.*, **147**, 495–517, <https://doi.org/10.1175/MWR-D-18-0140.1>.
- Knuteson, R.O., and coauthors, 2004: Atmospheric Emitted Radiance Interferometer. Part II: Instrument performance. *J. Atmos. Oceanic Technol.*, **21**, 1777-1789.
- Lin, Y., and K. E. Mitchell, 2005: The NCEP Stage II/IV hourly precipitation analyses: Development and applications. *19th Conf. on Hydrology*, San Diego, CA, Amer. Meteor. Soc., 1.2, https://ams.confex.com/ams/Annual2005/techprogram/paper_83847.htm
- Mlawer, E. J., S. J. Taubman, P. D. Brown, M. J. Iacono, and S. A. Clough, 1997: Radiative transfer for inhomogeneous atmospheres: RRTM, a validated correlated-k model for the longwave. *J. Geophys. Res.*, **102**, 16 663–16 682, <https://doi.org/10.1029/97JD00237>.
- NOAA/National Severe Storms Laboratory (NSSL). 2019. MRMS Merged Reflectivity Composite Quality Controlled Data. Version 1.0. UCAR/NCAR - Earth Observing Laboratory. <https://doi.org/10.26023/4551-7ZYL-Z00J>. Accessed 11 Jul 2023.
- Pearson, G., F. Davies, and C. Collier, 2009: An analysis of the performance of the UFAM pulsed Doppler lidar for observing the boundary layer. *J. Atmos. Oceanic Technol.*, **26**, 240-250.
- Privé, N. C., and R. M. Errico, 2013: The role of model and initial condition error in numerical weather forecasting investigated with an observing system simulation experiment. *Tellus*, **65A**, 21740, <https://doi.org/10.3402/tellusa.v65i0.21740>.

- Petersen, R.A., 2016: On the impact and future benefits of AMDAR observations in operational forecasts – Part 1: A review of the impact of automated aircraft wind and temperature reports. *Bull Amer Meteor. Soc.*, **97**, 585–602, doi:10.1175/BAMS-D-14-00055.1
- Petersen, R.A., L. Cronce, R. Mamrosh, R. Baker, and P. Pauley, 2016: On the impact and future benefits of AMDAR observations in operational forecasting – Part II: Water vapor observations. *Bull. Amer. Meteor. Soc.*, **97**, 2117–2133, doi:10.1175/BAMS-D-14-00211.1.
- Powers, J. G., and Coauthors, 2017: The Weather Research and Forecasting (WRF) Model: Overview, system efforts, and future directions. *Bull. Amer. Meteor. Soc.*, **98**, 1717–1737, <https://doi.org/10.1175/BAMS-D-15-00308.1>.
- Richard, E., A. Buzzi, and G. Zängl, 2007: Quantitative precipitation forecasting in the Alps: The advances achieved by the mesoscale alpine programme. *Quart. J. Roy. Meteor. Soc.*, **133**, 831–846, <https://doi.org/10.1002/qj.65>.
- Roberts, N. M., and H. W. Lean, 2008: Scale-selective verification of rainfall accumulations from high-resolution forecasts of convective events. *Mon. Wea. Rev.*, **136**, 78–97, <https://doi.org/10.1175/2007MWR2123.1>.
- Romine, G. S., C. S. Schwartz, C. Snyder, J. L. Anderson, and M. L. Weisman, 2013: Model bias in a continuously cycled assimilation system and its influence on convection-permitting forecasts. *Mon. Wea. Rev.*, **141**, 1263–1284, <https://doi.org/10.1175/MWR-D-12-00112.1>.
- Sandu, I., A. Beljaars, P. Bechtold, T. Mauritsen, and G. Balsamo, 2013: Why is it so difficult to represent stably stratified conditions in numerical weather prediction (NWP) models? *J. Adv. Model. Earth Syst.*, **5**, 117–133, doi:10.1002/jame.20013.
- Sato, K., J. Inoue, A. Yamazaki, J.-H. Kim, A. Makshtas, V. Kustov, M. Maturilli, and K. Dethloff, 2018: Impact on predictability of tropical and mid-latitude cyclones by extra Arctic observations. *Scientific Reports*, **8**(1), 12104. <https://doi.org/10.1038/s41598-018-30594-4>
- Schneider, R. S., and A. R. Dean, 2008: A comprehensive 5-year severe storm environment climatology for the continental United States. *24th Conf. on Severe Local Storms*, Savannah, GA, Amer. Meteor. Soc., 16A.4, https://ams.confex.com/ams/24SLS/techprogram/paper_141748.htm.

- Schwartz, C. S., G. S. Romine, M. L. Weisman, R. A. Sobash, K. R. Fossell, K. W. Manning, and S. B. Trier, 2015: A real-time convection-allowing ensemble prediction system initialized by mesoscale ensemble Kalman filter analyses. *Wea. Forecasting*, **30**, 1158–1181, <https://doi.org/10.1175/WAF-D-15-0013.1>.
- Schwartz, C. S., and R. A. Sobash, 2017: Generating probabilistic forecasts from convection-allowing ensembles using neighborhood approaches: A review and recommendations. *Mon. Wea. Rev.*, **145**, 3397–3418, <https://doi.org/10.1175/MWR-D-16-0400.1>.
- Schwartz, C. S., G. S. Romine, R. A. Sobash, K. R. Fossell, and M. L. Weisman, 2019: NCAR's real-time convection-allowing ensemble project. *Bull. Amer. Meteor. Soc.*, **100**, 321–343, <https://doi.org/10.1175/BAMS-D-17-0297.1>.
- Shao, H., and Coauthors, 2016: Bridging research to operations transitions: Status and plans of community GSI. *Bull. Amer. Meteor. Soc.*, **97**, 1427–1440, <https://doi.org/10.1175/BAMS-D-13-00245.1>.
- Sisterson, D.L., R.A. Peppler, T.S. Cress, P.J. Lamb, and D.D. Turner, 2016: The ARM Southern Great Plains (SGP) site. *The Atmospheric Radiation Measurement (ARM) Program: The First 20 years*. Monograph, 57, Amer. Meteor. Soc., 4.1-4.19, doi:10.1175/AMSMONOGRAPH-D-15-0054.1.
- Skamarock, W. C., and Coauthors, 2008: A description of the Advanced Research WRF version 3. NCAR Tech. Note NCAR/TN-475+STR, 113 pp., <https://doi.org/10.5065/D68S4MVH>.
- Snook, N., M. Xue, and Y. Jung, 2011: Analysis of a tornadic mesoscale convective vortex based on ensemble Kalman filter assimilation of CASA X-band and WSR-88D radar data. *Mon. Wea. Rev.*, **139**, 3446–3468, <https://doi.org/10.1175/MWR-D-10-05053.1>.
- Sobash, R. A., and D. J. Stensrud, 2015: Assimilating surface mesonet observations with the EnKF to improve ensemble forecasts of convection initiation on 29 May 2012. *Mon. Wea. Rev.*, **143**, 3700–3725, <https://doi.org/10.1175/MWR-D-14-00126.1>.
- Spuler, S. M., K. S. Repasky, B. Morley, D. Moen, M. Hayman, and A. R. Nehrir, 2015: Field-deployable diode-laser-based differential absorption Lidar (DIAL) for profiling water vapor. *Atmos. Meas. Tech.*, **8**, 1073–1087, <https://doi.org/10.5194/amt-8-1073-2015>.
- Spuler, S. M., M. Hayman, R. A. Stillwell, J. Carnes, T. Bernatsky, and K. S. Repasky, 2021: MicroPulse DIAL (MPD)—A diode-laser-based lidar architecture for quantitative

atmospheric profiling. *Atmos. Meas. Tech.*, **14**, 4593–4616, <https://doi.org/10.5194/amt-14-4593-2021>.

Stensrud, D. J., and Coauthors, 2013: Progress and challenges with Warn-on-Forecast. *Atmos. Res.*, **123**, 2–16, <https://doi.org/10.1016/j.atmosres.2012.04.004>.

Stillwell, R. A., S. M. Spuler, M. Hayman, K. S. Repasky, and C. E. Bunn, 2020: Demonstration of a combined differential absorption and high spectral resolution lidar for profiling atmospheric temperature. *Opt. Express*, **28**, 71–93, <https://doi.org/10.1364/OE.379804>.

Thompson, R. L., R. Edwards, J. A. Hart, K. L. Elmore, and P. Markowski, 2003: Close proximity soundings within supercell environments obtained from the Rapid Update Cycle. *Wea. Forecasting*, **18**, 1243–1261, [https://doi.org/10.1175/1520-0434\(2003\)018<1243:CPSWSE>2.0.CO;2](https://doi.org/10.1175/1520-0434(2003)018<1243:CPSWSE>2.0.CO;2).

Thompson, G., P. R. Field, R. M. Rasmussen, and W. D. Hall, 2008: Explicit forecasts of winter precipitation using an improved bulk microphysics scheme. Part II: Implementation of a new snow parameterization. *Mon. Wea. Rev.*, **136**, 5095–5115, <https://doi.org/10.1175/2008MWR2387.1>.

Torn, R. D., G. J. Hakim, and C. Snyder, 2006: Boundary conditions for limited area ensemble Kalman filters. *Mon. Wea. Rev.*, **134**, 2490–2502, <https://doi.org/10.1175/MWR3187.1>.

Trier, S. B., J. W. Wilson, D. A. Ahijevych, and R. A. Sobash, 2017: Mesoscale vertical motions near nocturnal convection initiation in PECON. *Mon. Wea. Rev.*, **145**, 2919–2941, <https://doi.org/10.1175/MWR-D-17-0005.1>.

Turner, D.D., and J.E.M. Goldsmith, 1999: Twenty-four-hour Raman lidar water vapor measurements during the Atmospheric Radiation Measurement program's 1996 and 1997 water vapor intensive observation periods. *J. Atmos. Oceanic Technol.*, **16**, 1062–1076.

Turner, D. D., and U. Löhnert, 2014: Information content and uncertainties in thermodynamic profiles and liquid cloud properties retrieved from the ground-based Atmospheric Emitted Radiance Interferometer (AERI). *J. Appl. Meteor. Climatol.*, **53**, 752–771, <https://doi.org/10.1175/JAMC-D-13-0126.1>.

Turner, D.D., and W.G. Blumberg, 2019: Improvements to the AERIoe thermodynamic profile retrieval algorithm. *IEEE J. Selected Topics Appl. Earth Obs. Remote Sens.*, **12**, 1339–1354, doi:10.1109/JSTARS.2018.2874968.

- UCAR/NCAR-Earth Observing Laboratory, 2019: NCAR/EOL Water Vapor DIAL Data, Version 1.0, UCAR/NCAR – Earth Observing Laboratory. Accessed July 2022. DOI: 10.26023/9Y30-6ASZ-YH04.
- Vogelmann, H., R. Sussmann, T. Trickl, and A. Reichert: Spatiotemporal variability of water vapor investigated using lidar and FTIR vertical soundings above the Zugspitze, *Atmos. Chem. Phys.*, **15**, 3135–3148, <https://doi.org/10.5194/acp-15-3135-2015>, 2015.
- Wang, X., D. M. Barker, C. Snyder, and T. M. Hamill, 2008: A hybrid ETKF–3DVAR data assimilation scheme for the WRF Model. Part I: Observing system simulation experiment. *Mon. Wea. Rev.*, **136**, 5116–5131, <https://doi.org/10.1175/2008MWR2444.1>.
- Weckwerth, T. M., J. W. Wilson, and R. M. Wakimoto, 1996: Thermodynamic variability within the convective boundary layer due to horizontal convective rolls. *Mon. Wea. Rev.*, **124**, 769–784.
- Weckwerth, T. M., 2000: The effect of small-scale moisture variability on thunderstorm initiation. *Mon. Wea. Rev.*, **128**, 4017–4030, [https://doi.org/10.1175/1520-0493\(2000\)129<4017:TEOSSM>2.0.CO;2](https://doi.org/10.1175/1520-0493(2000)129<4017:TEOSSM>2.0.CO;2).
- Weckwerth, T. M., K. J. Weber, D. D. Turner, and S. M. Spuler, 2016: Validation of a water vapor micropulse differential absorption lidar (DIAL). *J. Atmos. Oceanic Technol.*, **33**, 2353–2372, <https://doi.org/10.1175/JTECH-D-16-0119.1>.
- Wheatley, D. M., K. H. Knopfmeier, T. A. Jones, and G. J. Creager, 2015: Storm-scale data assimilation and ensemble forecasting with the NSSL experimental Warn-on-Forecast system. Part I: Radar data experiments. *Wea. Forecasting*, **30**, 1795–1817, <https://doi.org/10.1175/WAF-D-15-0043.1>.
- Whitaker, J. S., and T. M. Hamill, 2012: Evaluating methods to account for system errors in ensemble data assimilation. *Mon. Wea. Rev.*, **140**, 3078–3089, <https://doi.org/10.1175/MWR-D-11-00276.1>.
- Wulfmeyer, V., and Coauthors, 2011: The Convective and Orographically-induced Precipitation Study (COPS): The scientific strategy, the field phase, and research highlights. *Quart. J. Roy. Meteor. Soc.*, **137** (Suppl. 1), 3–30, <https://doi.org/10.1002/qj.752>.
- Wulfmeyer, V., R.M. Hardesty, D.D. Turner, A. Behrendt, M. Cadeddu, P. Di Girolamo, P. Schluessel, J. van Baelen, and F. Zus, 2015: A review of the remote sensing of lower tropospheric thermodynamic profiles and its indispensable role for the understanding and

simulation of water and energy cycles. *Rev. Geophys.*, 53, 819–895, doi:10.1002/2014RG000476.

Yang, Y., and X. Wang, 2023: Impact of radar reflectivity data assimilation frequency on convection-allowing forecasts of diverse cases over the Continental United States. *Mon. Wea. Rev.*, **151**(2), 341–362. <https://doi.org/10.1175/MWR-D-22-0095.1>

Zhang, J., K. Howard, and J. J. Gourley, 2005: Constructing three-dimensional multiple-radar reflectivity mosaics: Examples of convective storms and stratiform rain echoes. *J. Atmos. Oceanic Technol.*, **22**(1), 30–42. <https://doi.org/10.1175/JTECH-1689.1>

Zhang, F., Z. Meng, and A. Aksoy, 2006: Tests of an ensemble Kalman filter for mesoscale and regional-scale data assimilation. Part I: Perfect model experiments. *Mon. Wea. Rev.*, **134**, 722–736, <https://doi.org/10.1175/MWR3101.1>.